A NUMERICAL INVESTIGATION INTO THE PLASTIC BUCKLING PARADOX FOR CIRCULAR CYLINDRICAL SHELLS UNDER AXIAL COMPRESSION

Rabee Shamass[1], Giulio Alfano[1], Federico Guarracino[2]

1 - School of Engineering and Design, Brunel University, UB8 3PH Uxbridge, UK

2 – University of Naples 'Federico II', Via Claudio 21, 80125 Napoli, Italy

Abstract

It is widely accepted that for many buckling problems of plates and shells in the plastic range the flow theory of plasticity leads to a significant overestimation of the buckling stress while the deformation theory provides much more accurate predictions and is therefore generally recommended for use in practical applications. The present work aims to contribute to further understanding of the seeming differences between these two theories with particular regards to circular cylindrical shells subjected to axial compression. A clearer understanding of the two theories is established using accurate numerical examples and comparisons with some widely cited accurate physical test results. It is found that, contrary to common perception, by using a geometrically nonlinear finite element formulation with carefully determined and validated constitutive laws very good agreement between numerical and test results can be obtained in the case of the physically more sound flow theory of plasticity. The reasons underlying the apparent buckling paradox found in the literature regarding the application of deformation and flow theories and the different conclusions reached in this work are investigated and discussed in detail.

Keywords: shell buckling; shell instability; plastic buckling; deformation plasticity; flow plasticity; plastic paradox; non-linear FEA.

1. Introduction

Plastic buckling of circular cylindrical shells has been the subject of active research for many decades due to its importance to the design of aerospace, submarine, offshore and civil engineering structures. It typically occurs in the case of moderately thick

cylinders subjected to axial compression, external pressure, torsion or combinations of such loads. For example, buried pipelines used to transport fluids or pipelines resting on a deformed foundation can undergo high compressive axial loads, which can lead to axial buckling, or experience high external pressure leading to ovalisation buckling.

In general, the numerical analysis of plastic buckling of practical cylinders requires the determination of the nonlinear load-deflection path and must also consider bifurcation and mode changes. Therefore, an accurate prediction of the critical loads in the plastic range requires accounting for moderate large deflection and, one would expect, nonlinear, irreversible, path-dependent material behavior (Bushnell, 1982).

On the other hand, path-dependence is not always invoked as a necessary hypothesis for modeling purposes. In fact, based on whether path-dependence is accounted for or not, the plasticity models that have been proposed for metals in the strain hardening range can be divided into two groups: the 'deformation theory' of plasticity and the 'flow theory' of plasticity. In both of these theories the plastic deformations do not allow volume changes as plastic yielding is governed by the second invariant J_2 of the deviatoric part of the stress tensor, whereby in this respect they are both so-called J_2 theories. However, the deformation theory of plasticity is based on the assumption that for continued loading the state of stress is uniquely determined by the state of strain and, therefore, it is a special class of path-independent non-linear elasticity constitutive laws. According to this assumption, after a strain reversal, rather than recovering the initial elastic stiffness, as is found in physical tests, the initial loading curve is followed. On the other hand, the flow theory of plasticity assumes that an (infinitesimal) increment of stress is uniquely determined by the existing strain and its increment. This leads to a path-dependent relationship in which the current stress depends not only on the value of the current total strain but also on how the actual strain value has been reached, thus making the constitutive relationship path dependent.

There is a general agreement among engineers and researchers that the deformation theory of plasticity lacks physical rigour in comparison to the flow theory. Use of the deformation theory predicts buckling loads that are less than corresponding loads obtained with the incremental theory, and evidence of comparison between measured and calculated buckling loads points in favour of deformation theory results. This fact may be related to several factors and Onat and Drucker (1953) first pointed out through an approximate analysis that buckling predictions based on the flow theory for long

plates supported on three sides tend to those predicted by the deformation theory if small but unavoidable imperfections are taken into account. Later, this so called "plate buckling paradox" was theoretically examined by Sewell (1963) who obtained lower flow theory buckling loads by allowing a variation in the direction of the unit normal. In a subsequent study Sewell (1973) also illustrated that the use of Tresca yield surface in the flow theory of plasticity leads to significant reductions in the buckling loads. An extensive discussion of the buckling paradox as understood at that time was given by Hutchinson (1974).

More recently, Wang and Huang (2009) examined the elastoplastic buckling of a rectangular plate made of alloy Al 7075 T6, typically used in the aerospace industry, subjected to biaxial loading (uniform compressive load $\sigma_2 = -\sigma$ in one direction and tension or compression load $\sigma_1 = \xi\sigma$ in the perpendicular direction, where ξ is a constant). A detailed parametric study was made using the differential quadrature method (DQ) and the authors concluded that the small deformation assumption used to establish the governing differential equation could possibly be the reason for the large discrepancy between the results obtained using either deformation or flow theory. In a later paper, Wang and Zhang (2011) used the DQ method to obtain the elastoplastic buckling stresses for thick rectangular plates with various values of the thickness-to-side-length ratio, and for various material properties and boundary conditions. They found that the discrepancy in the calculated buckling stresses between the two theories of plasticity gets larger with increasing plate thickness, the ratio E/σ_y and exponent n in the Ramberg–Osgood expression, where E and σ_y are the Young's modulus and yield strength. They suggested that another explanation of the discrepancies in the results using the two theories for thick plates could be that the deformation theory predicts an increasingly lower in-plane shear modulus as the level of plasticity increases, which results in lower calculated buckling-stress values.

Restricting attention to the plastic buckling of circular cylindrical shells, Mao and Lu (1999) analytically examined simply supported cylinders made of aluminium alloy subjected to axial compression load. They compared the buckling stresses predicted by their analytical formula with the experimental results conducted by Lee (1962) and found that the deformation theory provides closer results with the tests while the flow theory significantly over-predicts the critical loads.

Blachut et al. (1996) conducted experimental and numerical analyses of 30 mild-steel machined cylinders, of different dimensions, subject to axial tension and increasing external pressure. They showed that agreement between the buckling stresses calculated using the two theories was strongly dependent on the ratio of the length L of the cylindrical shell to its outer diameter D. For short cylinders ($L/D \leq 1$) the plastic buckling pressure predicted by flow or deformation theory coincided only when the tensile axial load vanished. By increasing the axial tensile load, the plastic buckling pressure calculated using by the flow theory of plasticity quickly diverged from corresponding values calculated using the deformation theory, which were closer to the experimental values. For specimens with L/D ranging from 1.5 to 2 the results predicted by both theories were very similar for a certain range of combined loading, beyond which the values calculated using the flow theory began to deviate from the corresponding results using the deformation theory and became unrealistic in correspondence of large plastic strains.

Durban and Ore (1992) analytically investigated the buckling of axially compressed circular cylindrical shells in the plastic range for various boundary conditions. Similar to Mao and Lu (1999), they concluded that the buckling compression stresses predicted by the deformation theory appeared to be in good agreement with measured test results, while those provided by the flow theory overestimated the measured test values. Moreover, the authors observed that the differences between the theoretical results predicted by the flow and deformation theory reduced with increasing value of the strain hardening parameter.

Bardi and Kyriakides (2006) tested fifteen cylindrical stainless steel tubes, with D/t ranging between 23 and 52, under axial compression and determined the critical stresses and strains at the onset of wrinkling. They reported the buckling modes, including the number and the size of waves. They also calculated the same quantities analytically using the deformation or the flow plasticity theory. The calculations included the effects of assuming both isotropic and anisotropic material behaviour. Bardi and Kyriakides concluded that the flow theory significantly over-predicts the critical stresses and strains while the deformation theory leads to critical stress and strain in better agreement with the experimental results. Moreover, the flow theory grossly over-predicted the wavelength of wrinkles while the deformation theory was in better agreement with the wavelengths measured in the tests.

The plastic paradox does not seem to be limited to the buckling of plates and cylinders. For example, Galletly el al. (1990) investigated the plastic buckling of six machined steel torispherical domes of different geometries and subjected to internal pressure. The tests were carried out to highlight the differences in buckling stresses calculated, using the code BOSOR 5 (Bushnell, 1986), with either the flow or the deformation theory. They measured low-amplitude waves in the knuckle of the torispherical domes by probes allocated at the knuckle region for all six specimens. These waves grew with the increasing internal pressure in four test specimens and became visible to the naked eye while in other two specimens the waves could not be visually detected but could be felt by finger-tip contact. In their analysis they found that, for all the tests, the buckling mode failure and the internal pressure predicted by the deformation theory was in good agreement with the experimental results, the difference varying between 6% and 29%. On the other hand, the flow theory did not predict a buckling failure mode for any of the four test specimens.

In the framework provided by the above cited publications, the present work aims to shed light on the plastic buckling paradox by conducting accurate linear and nonlinear finite-element modelling of buckling of cylindrical shells using the flow theory and the deformation theory of plasticity.

Attention is focused on cylindrical shells subject to axial compression with outer-radius-to-thickness ratio R/t ranging between 9 and 120, because of the great significance of this geometry and loading conditions for engineering application. The predictions have been compared with widely recognised experimental results reported in the literature by Lee (1962) and Batterman (1965) and with the analytical results reported by Mao and Lu (1999) and Durban and Ore (1992).

It is found that, in contrast to common understanding, by using carefully validated geometrically nonlinear finite element (FE) modelling a very good agreement between numerical and experimental results can be obtained in the case of the physically sound flow theory of plasticity. The reasons underlying the apparent buckling paradox are then investigated and discussed in detail.

2. Test samples and finite-element modelling

2.1 Geometry and elements

The plastic buckling of perfect and imperfect cylinders subjected to axial compression has been numerically simulated using non-linear FE analyses using both the flow and the deformation theory of plasticity, adopting the FE code ABAQUS, version 6.11-1. Specific attention has been paid to adopt model parameters which, in the case of proportional monotonic (increasing) loading, result in the same stress-strain curve in both theories, to within a negligible numerical error. The FE simulations were conducted for aluminium cylinders tested by Lee (1962) and Batterman (1965). Out of the ten cylinders tested by Lee and of the thirty cylinders tested by Batterman, eight and nine of them, respectively, were chosen for the numerical investigation. The criterion used for the selection of these tests was to account for a wide range of R/t. The results of the analysis are compared with the corresponding test results reported by the above authors and with analytical results derived by Durban and Ore (1992) and Mao and Lu (1999).

In Lee's experiments, the specimens were made of cylinders of aluminium alloy 3003-0, which were reported to be free of residual stresses. The compression pad used to transfer the axial force and the base block had annular recesses in which the specimens were inserted. Lee tested 10 cylinders with an outer diameter of 101.6 mm and radius-thickness ratios R/t varying between 9.36 and 46.06. He pointed out that the imperfections in general were irregular such that the cross sections had somewhat oval shapes. Eight cylindrical shells were chosen for the present numerical analysis, as illustrated in Table 2.1.

The end sections during the test were neither perfectly hinged nor perfectly clamped. Therefore, the two idealised boundary conditions, hinged and clamped, were modelled separately. For the case of clamped ends, the bottom edge of the shell was considered as fully fixed, i.e. with no allowed translations and rotations for all degrees of freedom; the other edge was also considered fully restrained, except for the displacement in the axial direction which was prescribed to increase monotonically downward. In the case of hinged ends, the rotations normal to the cylinder wall were fully allowed.

The cylindrical specimens were modelled using a general purpose 4-noded shell element which has six degrees of freedom at each node. This element is named "S4" in the commercial software ABAQUS and is based on a thick shell theory. The shell formulation accounts for finite membrane strains, therefore this element can be used to perform large strain analyses. The element is widely used for industrial applications because it is suitable for both thin and thick shells. The S4 element uses a normal integration rule with four integration points. The enhanced-strains approach is employed to prevent shear and membrane locking. Among the ABAQUS elements, S4 outperforms S4R as the former evaluates more accurately the membrane strains, which plays a key role in the problem at hand (Simulia, 2011).

Spec.	R (mm)	R/t	L/R	t (mm)	L (mm)	Imperfection ratio δ/t
A330	50.8	9.36	4.21	5.43	213.87	0.012
A230	50.8	9.38	6.32	5.42	321.01	0.012
A130	50.8	9.39	10.5	5.41	533.40	0.012
A320	50.8	19.38	4.1	2.62	208.28	0.03
A220	50.8	19.4	6.15	2.62	321.10	0.05
A310	50.8	29.16	4.06	1.74	206.25	0.045
A110	50.8	29.22	10.16	1.74	516.13	0.033
A300	50.8	46.06	4.04	1.1	205.23	0.105

Table 2.1: Geometry and imperfection ratio of the aluminium cylinders tested by Lee (1962).

A structured mesh was used, made from a number of divisions along the circumference and longitudinal direction reported in Table 2.2 for each specimen.

	Specimens							
Number of elements	A330	A230	A130	A320	A220	A310	A110	A300
- **around the circumference**	150	150	150	150	150	150	150	150
- **along the length**	100	150	250	98	150	97	242	96

Table 2.2: FE mesh discretisation adopted for the FE analyses of the cylinders tested by Lee.

In the tests carried out and reported by Batterman (1965), the specimens were made of cylinders of aluminium alloy 2024-T4. The ends of the specimens were restrained such as to be considered clamped. Batterman tested 30 cylinders with

radius-thickness ratio R/t varying between 9.7 and 121.25. Nine cylindrical shells were chosen for the present numerical analysis, as presented in Table 2.3.

Spec.	R (mm)	R/t	L/R	t (mm)	L (mm)
12	34.79	9.7	2.92	3.586	101.6
18	34.8	9.76	2.92	3.566	101.6
22	35.56	13.93	0.72	2.553	25.4
5	33.42	25.94	0.76	1.297	25.4
15	34.72	44.69	1.47	0.777	50.8
16	34.59	56.52	0.73	0.612	25.4
26	34.49	85.95	0.74	0.4013	25.4
8	33.2	114.56	1.53	0.29	50.8
9	33.12	116.61	0.77	0.284	25.4

Table 2.3: Geometries of aluminium cylinders tested by Batterman (1965).

Again 4-noded shell (S4) elements were used in the FE modelling with a structured mesh with numbers of elements along circumference and length shown in Table 2.4 for each specimen.

	Specimens								
Number of elements	12	18	22	5	15	16	26	8	9
- **around the circumference**	150	150	250	250	150	250	250	250	250
- **along the length**	70	70	28	30	35	29	29	61	31

Table 2.4: FE mesh discretisation adopted for the analyses of the cylinders tested by Batterman.

2.2 Constitutive relationship and material constants

The uniaxial stress-strain relationship of the material under monotonic loading was characterised by the Ramberg-Osgood relationship:

$$E\varepsilon = \sigma + \alpha\left(\frac{\sigma}{\sigma_y}\right)^{n-1}\sigma \tag{2.1}$$

where ε and σ denotes uniaxial strain and stress, E and ν are Young's modulus and Poisson's ratio, respectively, σ_y is the nominal yield strength, sometimes called 'proof stress' and denoted by $\sigma_{0.2\%}$ (see Figure 2.1), α is the 'yield offset' and n is the strain hardening parameter.

The Ramberg-Osgood input parameters used in the numerical simulations are reported in Table 2.5.

	E [GPa]	σ_y[MPa]	ν	n	α
Lee's tests	70	23.62	0.32	4.1	0.4286
Batterman's tests	74.463	389.554	0.32	14.45	0.3823

Table 2.5: Ramberg-Osgood constants used in the numerical analyses.

For the cylinders tested by Lee (1962), the parameters used for the FE modelling are those reported by Lee's paper. For Batterman's tests two sets of experimental data from tensile and compression tests were reported by the author and fitted with the Ramberg-Osgood relationship. In particular, two values of the yield strength, $\sigma_{0.2\%}$ and $\sigma_{0.5\%}$, corresponding to strains of 0.2% and 0.5%, respectively, measured in tensile and compression tests were reported by Batterman (1965) and were used to calculate the values of α and n reported in Table 2.6. In particular, since $\sigma_y = \sigma_{0.2\%}$, from Equation (2.1) one has:

$$\alpha = 0.002 \, \frac{E}{\sigma_y} \tag{2.2}$$

and n is obtained from the relationship:

$$n = \frac{ln\left(\frac{0.005\, E}{\alpha\, \sigma_y}\right)}{ln\left(\frac{\sigma_{0.5\%}}{\sigma_y}\right)} \tag{2.3}$$

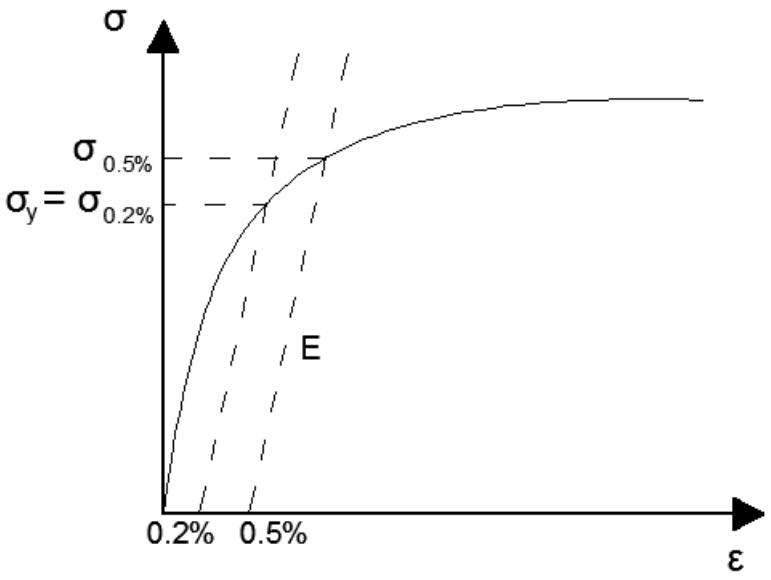

Figure 2.1: Illustration of $\sigma_{0.2\%}$ and $\sigma_{0.5\%}$ on the stress-strain curve.

Data from	Compression tests	Tension tests
E [GPa]	74.463	73.57
$\sigma_{0.2\%}$ [MPa]	389.55	408.86
$\sigma_{0.5\%}$ [MPa]	415.06	419.2
α	0.3823	0.3599
n	14.45	36.68

Table 2.6: Material constants from tensile and compression tests (Batterman, 1965).

Figure 2.2 shows a comparison between the experimental uniaxial stress-strain curves reported by Batterman and those obtained using the Ramberg-Osgood relationship with the parameters in Table 2.6. It can be seen that the Ramberg-Osgood constants calculated using the compression tests lead to a very good agreement with the experimental compression data, such that they have been used for the numerical analyses.

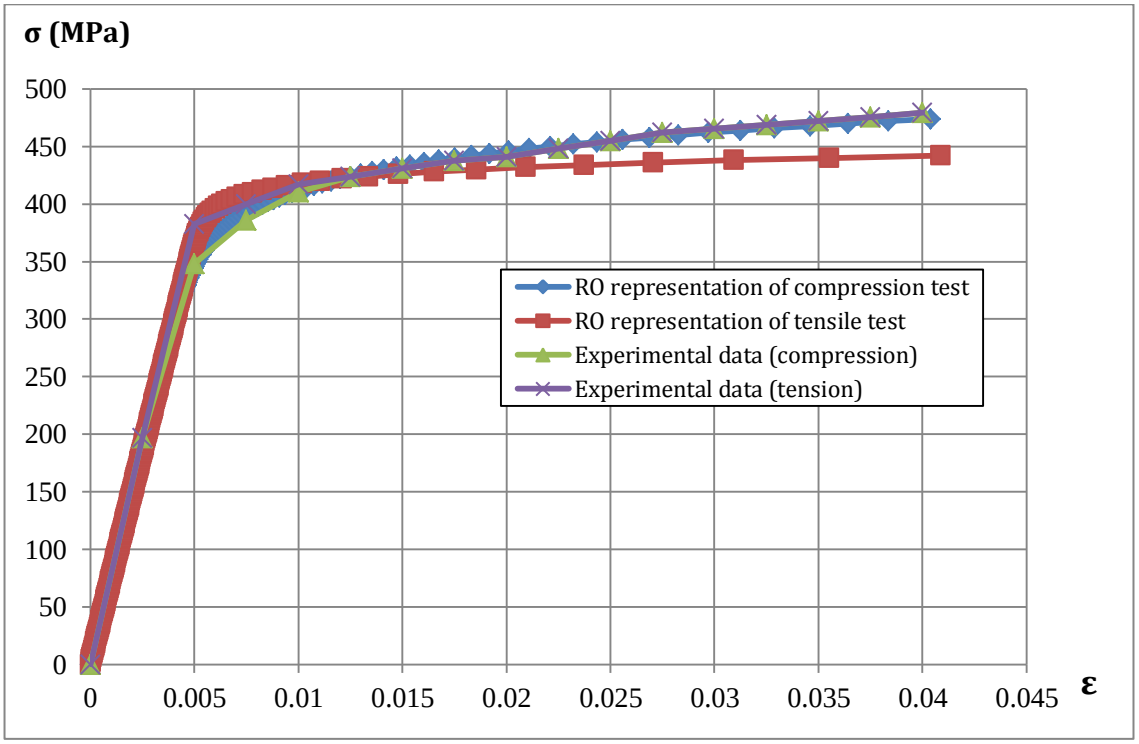

Figure 2.2: Comparison between experimental and formula curves

The deformation theory of plasticity used in the numerical simulations is obtained by extending the Ramberg-Osgood law to the case of a multi-axial stress state using the von Mises formulation (J_2 theory) and results in the following path-independent relationship (Simulia, 2011). The resulting equations are reported in Appendix A1.

The flow theory used in the numerical simulations was the classical J_2 flow theory of plasticity, with nonlinear isotropic hardening and in the small-strain regime (Simo and Hughes, 1998; Simulia, 2011). Such theory is implemented in a model available in ABAQUS. For the sake of completeness the equations governing the theory are reported in Appendix A2. On the other hand, it is important to underline here that the input data for the flow theory were obtained in such a way that the same stress-strain curve as in the case of the deformation theory is obtained for the case of uniaxial stress and monotonic loading, to within a negligibly small numerical tolerance.

It is worth recalling that the Ramberg-Osgood relationship does not account for any initial linearly elastic behaviour but represents a nonlinear material response for any value of the stress, even if for relatively small stress values the deviation from linearity is quite small. Hence, the function $\bar{\sigma}$ in Equation (A.4) should be such that $\bar{\sigma}(0) = 0$, i.e. the initial yield stress in the flow theory should be taken as zero. However, the numerical implementation of the J_2 flow theory requires the use of the well-known radial-return algorithm (see (Simo and Hughes, 1998) among many others) which, in turn, requires the calculation of the unit normal vector to the yield surface. The unit normal vector is undefined if the yield surface degenerates to a point, which is why, using the J_2 flow theory implemented in ABAQUS, a zero value of $\bar{\sigma}(0)$ leads to lack of convergence in the first increment. Hence, the value $\bar{\sigma}(0) = 10^{-5}$ MPa was assumed. Furthermore, a tabulated approximation of $\bar{\sigma}\left(\varepsilon_p^{eq}\right)$ was obtained by considering $\bar{\sigma}$ increments of 2 MPa; for each value of the stress $\bar{\sigma}$ the corresponding equivalent plastic strain value ε_p^{eq} was obtained from Equation (2.1) as follows

$$\varepsilon_p^{eq} = \alpha \left(\frac{\bar{\sigma}}{\sigma_y}\right)^{n-1} \frac{\bar{\sigma}}{E} \tag{2.4}$$

Figure 2.3 illustrates the load-displacement curves obtained for the numerical tensile test of a square rod of 10×10 mm^2 subject to homogeneous uniaxial stress using both plasticity theories in conjunction with the material parameters used for the simulation of Lee's tests. It can be appreciated that the load-deflection curves are

identical during the loading process. Upon unloading, in the case of the deformation theory the same loading curve is followed, whereas in the case of the flow theory, the unloading is elastic. In the case of the flow theory, in order to restore the value of deflection to zero, a compressive load is applied and the load-deflection path proceeds as shown in Figure 2.3. The same procedure has been followed for the material models used to simulate Batterman's tests, which led to a perfectly analogous graph as in Figure 2.3.

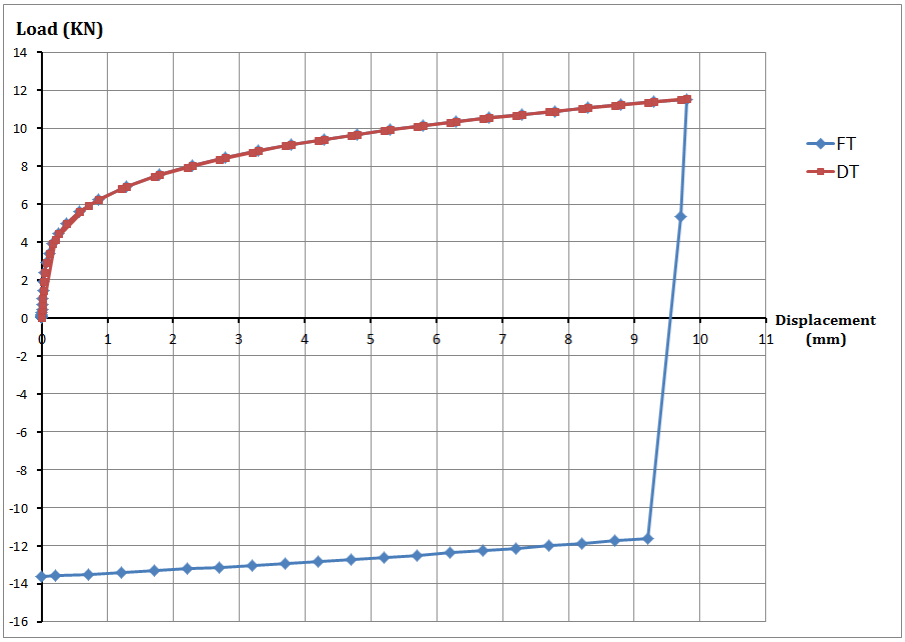

Figure 2.3: Load-displacement relation for a 10×10 mm^2 square rod of aluminium alloy 3003-0 subjected to homogeneous uniaxial stress.

It is worth remarking that the nonlinear isotropic model used for the flow theory of plasticity obviously does not account for the Baushinger effect, but plastic strain reversal always occurred in the simulations considered here after the maximum (buckling) load had been reached, so that ignoring the Baushinger effect does not affect the buckling problems under analysis.

2.3 Large displacement formulation

The above constitutive relationships are extended to the large-strain regime by using spatial co-rotational stress and strain measures and a hypo-elastic relation between the rates of stress and elastic strain (Simulia, 2011). This has been the subject of controversial debate because hypo-elastic laws lead to fictitious numerical

dissipation (Simo and Hughes, 1998). However, this large-strain formulation is widely implemented in many commercial codes, including ABAQUS, and it is generally accepted that the hypo-elasticity of the formulation has limited influence on the results because, even when strains are large, the elastic part of the strain is typically still very small and therefore close to the limit where hypo-elastic and hyper-elastic formulations coincide (Simo and Hughes, 1998).

2.4 Solution strategy

The nonlinear analysis was conducted using the modified Riks' approach (Riks, 1979) to trace the nonlinear response. Riks' method was the first of the so-called "arc-length" techniques, which provide an incremental approach to the solution of problems involving limit points in the equilibrium path. In this technique, both the vector of displacement increments $\Delta\mathbf{u}$ and the increment $\Delta\lambda$ of the scalar multiplier of the applied loads or displacements are unknown variables in the incremental/iteration scheme. The Riks' formulation iterates along a hyper plane orthogonal to the tangent of the arc-length from a previously converged point on the equilibrium path (Falzon, 2006). The iterations within each increment are performed using the Newton–Raphson method; therefore, at any time there will be a finite radius of convergence (Simulia, 2011).

In this analysis, the displacement at the top edge of the cylinder is prescribed to be equal to $\lambda\,\mathbf{u}_0$, where $\mathbf{u}_0$ denotes a reference downward vertical displacement and λ is the scalar multiplier . The analysis accounts for geometrical non-linearity as discussed in Sections 2.1 and 2.3. The critical load is determined by the point at which the load-shortening curve reaches a maximum.

The machine compliance was not included in the analyses reported because it does not affect the computed buckling stresses and only results in a right-ward shift of the load-shortening curves. This was confirmed by additional analyses, not reported here, in which the compliance was introduced with suitably inserted springs at the top edge.

2.5 Imperfection sensitivity analysis

In order to study the imperfection sensitivity of the cylinders, in the case of Lee's tests the analysis was carried out both for perfect cylinders and for two reference values of maximum imperfection amplitude, equal to 10% and 20% of the thickness.

Moreover, the analysis was also conducted for the imperfection amplitudes presented in Table 2.1, experimentally measured by Lee (1962).

In the case of Batterman's tests, the analysis was carried out both for perfect cylinders and for two reference values of imperfection amplitude, i.e. 5% and 10% of the thickness.

In both cases, imperfections were modelled by scaling the first linear buckling eigenmode and adding it to the perfect cylinder (see Figures 2.4 and 2.5). The linear buckling analysis has been conducted assuming linear elastic material behaviour and small displacements.

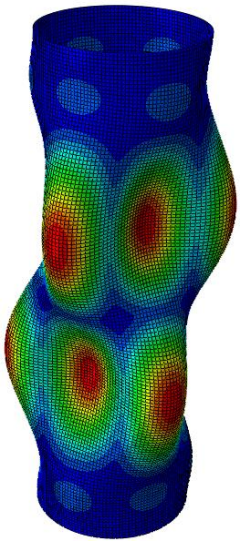

First Eigenmode for A220 cylinder

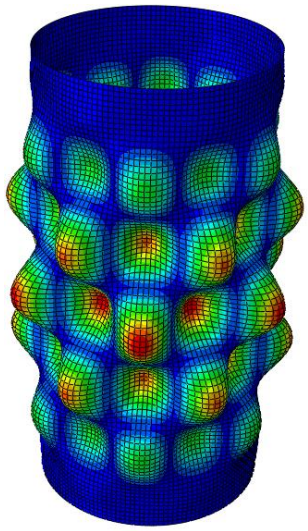

First Eigenmode for A300 cylinder

Figure 2.4: Buckling eigenmodes used in the simulation of Lee's tests to account for imperfections.

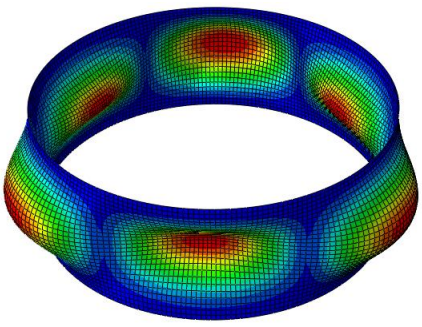

First Eigenmode for sp.22 cylinder

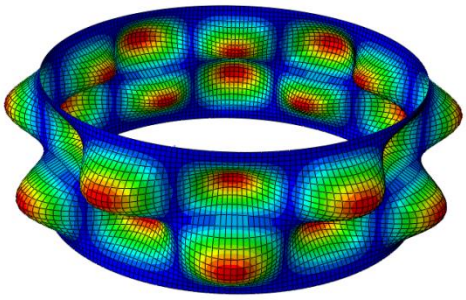

First Eigenmode for sp.16cylider

Figure 2.5: Buckling eigenmodes used in the simulation of Batterman's tests to account for imperfections.

3. FEA results for Lee's specimens

As mentioned earlier, due to the uncertainty regarding the actual boundary conditions, both perfectly hinged and perfectly clamped conditions were considered at the ends of the specimens. With hinged boundary conditions applied to the perfect model, wrinkles developed in an axisymmetric fashion as shown in the Figure 3.2. However, for clamped edges Figures 3.1 - 3.3 show that the deformed shapes of model appear to correspond well with the test results. Moreover, Table 3.1 shows that, for flow and deformation theory, the clamped boundary conditions resulted in a closer agreement between numerically calculated and experimentally measured plastic buckling stresses than in the case of hinged boundary conditions. This suggests that the actual test arrangement by Lee should be considered to prevent radial displacements and rotations at both ends of the specimens

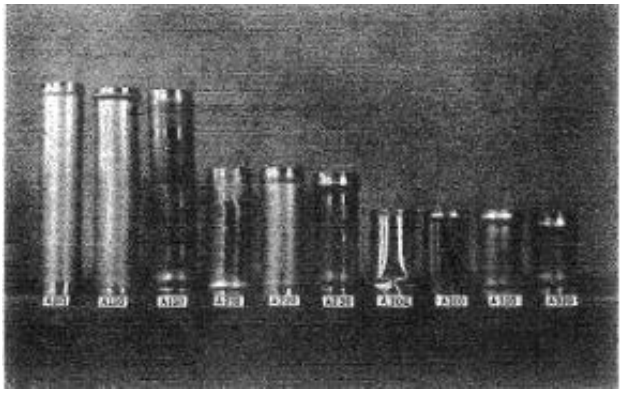

Figure 3.1: Buckling mode failure predicted experimentally (Lee, 1962) (reprinted by kind permission of the American Institute of Aeronautics and Astronautics, Inc).

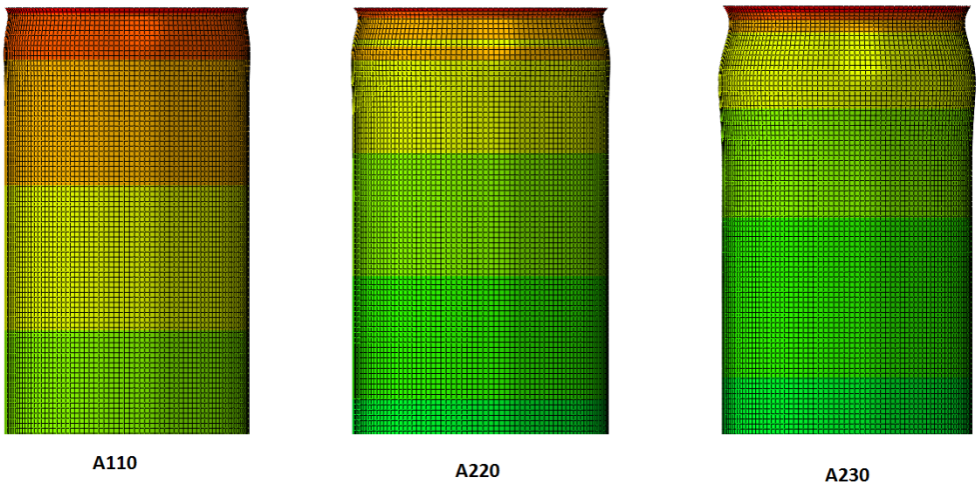

Figure 3.2: Axisymmetric deformation of axial compression shells with hinged boundary conditions and without initial imperfection

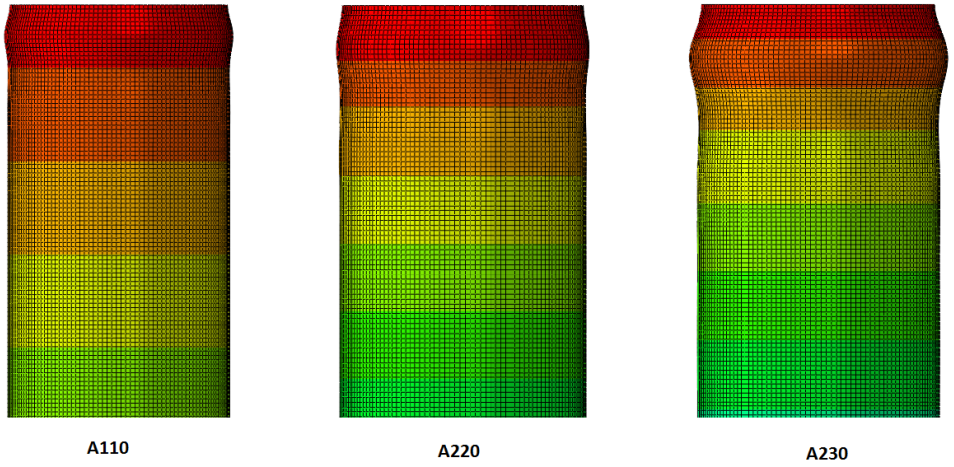

Figure 3.3: Axisymmetric deformation of axial compression shells with clamped boundary conditions and without initial imperfection.

Figures 3.4 and 3.5 show that the buckling stresses calculated using flow and deformation theory in the simulation of Lee's tests have a low sensitivity to the imperfection amplitude for moderately thick shells. However, both theories show an increase in the imperfection sensitivity with increasing R/t ratios.

Table 3.2 shows that the results calculated using the flow theory are in better agreement with the measured test results than those using the deformation theory. In fact, the buckling stresses calculated using the deformation theory tend to fall below the experimental values for all specimens except A310. In the case of the flow theory, on the contrary, numerical and experimental values generally are within a 3% discrepancy, with no clear pattern. The only cases in which the buckling stresses are under-estimated by the flow theory are for specimens A110 and A300, and in such cases the difference with the experiments were 2% and 9% respectively, generally well below the 9% and 21% differences which occurred for the same cases when the deformation theory was used.

Figures 3.6-3.7 show the load-displacement curves resulting from flow and deformation plasticity for specimens A230 and A300, respectively. It can be seen that the curve predicted by flow theory is always above the curve predicted by deformation theory for all cases. The load-displacement curves obtained for all other specimens are very similar to those in Figures 3.6 and 3.7 and therefore have not been reported.

Spec.	Experimental Buckling Stress (Lee , 1962)	Numerical Analysis (ABAQUS)-simply supported edges				Numerical Analysis (ABAQUS)-clamped edges			
		Flow Plasticity		Deformation Plasticity		Flow Plasticity		Deformation Plasticity	
		Buckling Stress (Mpa)	P_{expt}/P_{ABAQUS}	Buckling Stress (Mpa)	P_{expt}/P_{ABAQUS}	Buckling Stress (Mpa)	P_{expt}/P_{ABAQUS}	Buckling Stress (Mpa)	P_{expt}/P_{ABAQUS}
A330	96.87	81.64	1.19	75.52	1.28	98.58	0.98	88.82	1.09
A230	97.22	81.40	1.19	75.43	1.29	97.84	0.99	88.74	1.10
A130	94.6	81.3491	1.16	75.47	1.25	97.83	0.97	88.89	1.06
A320	78.6	62.30	1.26	59.94	1.31	80.48	0.98	74.10	1.06
A220	81.15	62.30	1.30	60.27	1.35	80.85	1.00	73.90	1.10
A310	64.74	54.79	1.18	53.31	1.21	72.47	0.89	66.84	0.97
A110	74.12	54.81	1.35	53.16	1.39	72.94	1.02	66.84	1.11
A300	69.71	47.64	1.46	47.11	1.48	64.25	1.08	59.16	1.18

Table 3.1: Results obtained with hinged and clamped boundary conditions for both deformation and flow theory of plasticity, in comparison with the corresponding test results by Lee (1962).

Spec.	Experimental Buckling Stress (Lee , 1962)	Imperfection ratio δ/t	Numerical Analysis (ABAQUS)					
			Flow Plasticity			Deformation Plasticity		
			Buckling Stress (Mpa)	P_{expt}/P_{ABAQUS}	Mode of failure	Buckling Stress (Mpa)	P_{expt}/P_{ABAQUS}	Mode of failure
A330	96.87	0.012	98.54	0.98	AX, Ring-Shaped near the edges	89.05	1.09	*AX, 4*LW
A230	97.22	0.01	97.84	0.99	AX, Ring-Shaped near the edges	88.74	1.10	AX, 6LW
A130	94.6	0.01	97.82	0.97	AS, Ring-Shaped near the edges	88.32	1.07	*AS, 6LW near the edges
A320	78.6	0.03	80.48	0.98	AX, Ring-Shaped near the edges	74.10	1.06	AX, 5LW
A220	81.15	0.05	80.84	1.00	AX, Ring-Shaped near the edges	73.90	1.10	AS, 8LW
A310	64.74	0.05	71.54	0.90	AS, Ring-Shaped near the edges	66.59	0.97	AS, 6LW
A110	74.12	0.03	72.94	1.02	AS, Ring-Shaped near the edges	66.84	1.11	AS, 6LW near the edges
A300	69.71	0.11	64.16	1.09	Ring-Shaped near the edges and gentle DM pattern in the central region	57.44	1.21	Ring-Shaped near the edges and gentle DM pattern in the central region

* AX-Axisymmetric buckling wave * AS- Almost axisymmetric buckling wave * DM-Diamond shaped buckling wave * LW- number of longitudinal waves

Table 3.2: Compression between test and numerical results for both flow and deformation theory of plasticity (imperfections identified by Lee (1962))

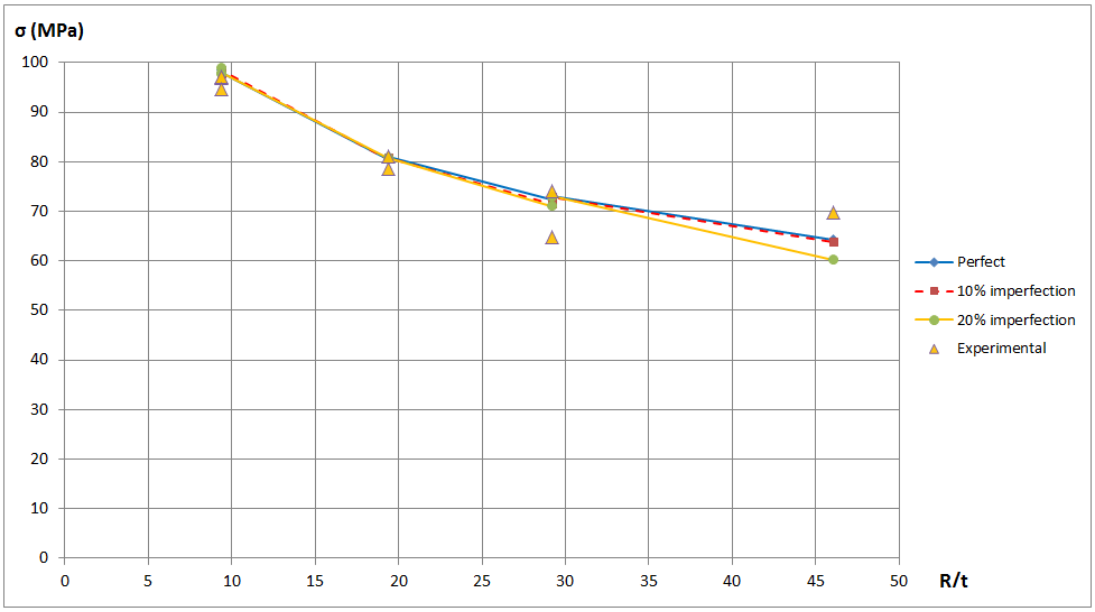

Figure 3.4: Effect of imperfections on the buckling load calculated using the flow theory of plasticity

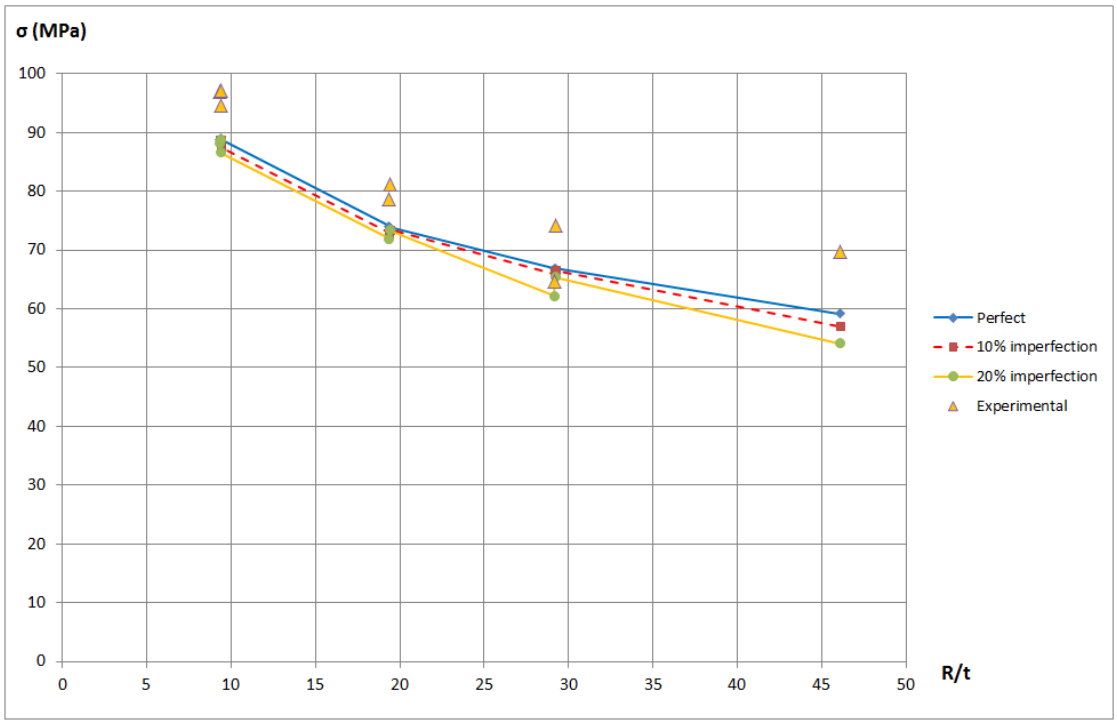

Figure 3.5: Effect of imperfections on the buckling load calculated using the deformation theory of plasticity

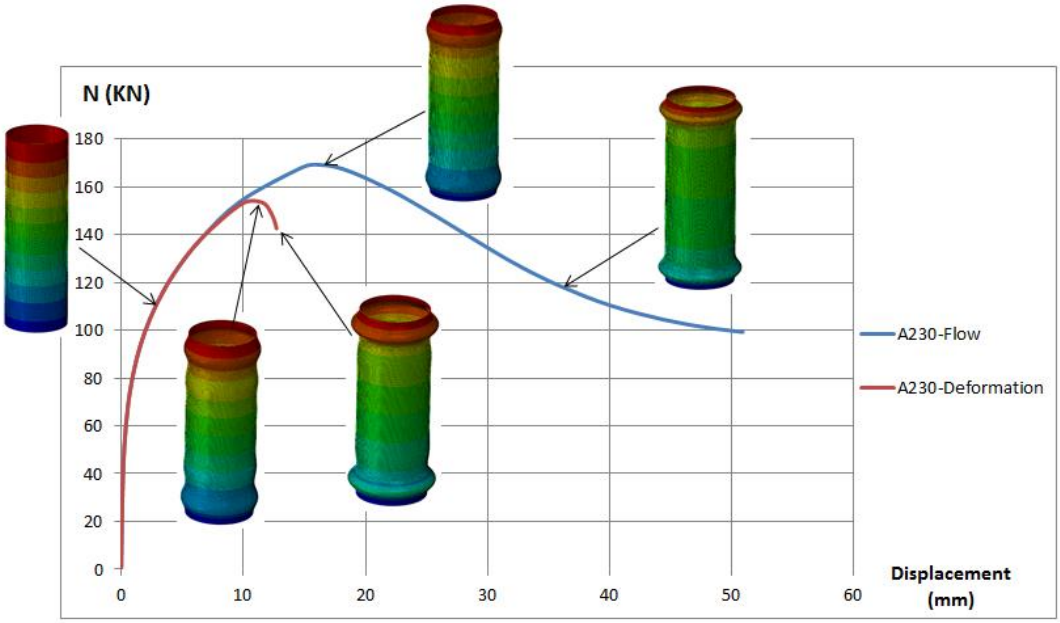

Figure 3.6: Axial load vs. prescribed displacement for specimen A230 for flow and deformation theories.

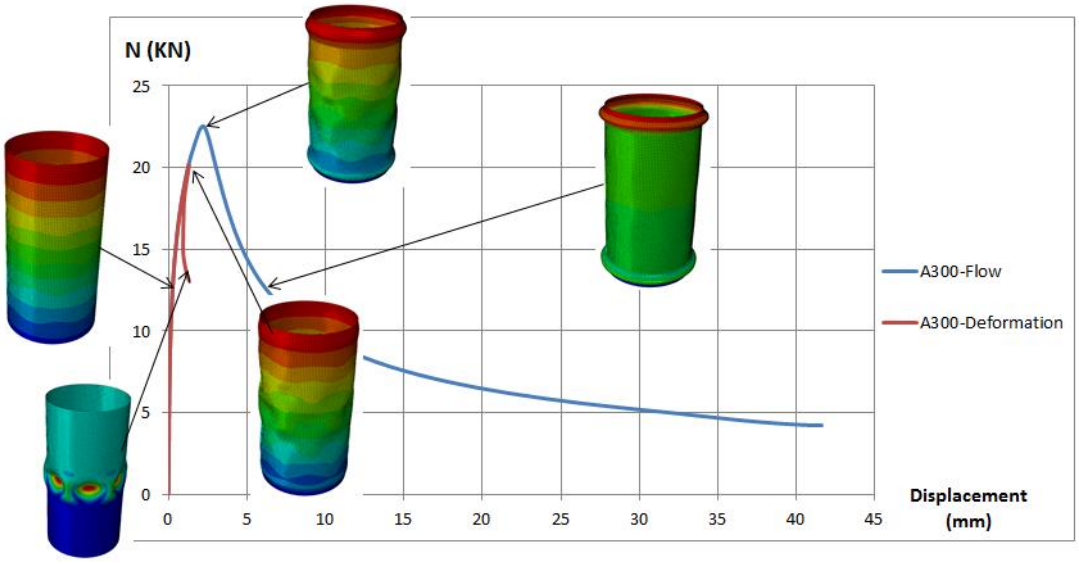

Figure 3.7: Axial load vs. prescribed displacement for specimen A300 for flow and deformation theories.

Lee's tests were studied analytically by Durban and Ore (1992) and Mao and Lu (1999) under the assumption of axisymmetric buckling. The results of their calculations, illustrated in Table 3.3 and 3.4, show that the deformation theory results in better agreement with the findings by Lee (1962) and that the flow-theory predictions systematically over estimate the buckling stresses. This is in contrast with the results of the present study, which show that, if appropriately applied, the flow theory accurately estimates the experimental buckling stress.

Spec.	Experimental Buckling Stress (Mpa)	Analytical (Mao and Lu, 1999)		Numerical Analysis (ABAQUS)	
	(Lee , 1962)	Flow	Deformation	Flow	Deformation
A330	96.87	165.46	89.71	98.58	88.82
A320	78.60	124.25	74.87	80.48	74.10
A310	64.74	106.00	67.70	72.47	66.84

Table 3.3: Comparison between results Mao and Lu (1999) and present numerical results for both flow and deformation theories of plasticity

Spec.	Experimental Buckling Stress (Mpa) (Lee , 1962)	Analytical (Ore and Durban, 1992)		Numerical Analysis (ABAQUS)	
		Flow	Deformation	Flow	Deformation
A330	96.87	162.32	88.34	98.58	88.82
A230	97.22	162.32	88.34	97.84	88.74
A130	94.6	161.59	87.81	97.83	88.89
A320	78.6	121.74	73.26	80.48	74.10
A220	81.15	121.51	72.80	80.85	73.90
A310	64.74	107.73	66.79	72.47	66.84
A110	74.12	107.64	66.52	72.94	66.84
A300	69.71	87.26	59.25	64.25	59.16

Table 3.4: Comparison between results by Durban and Ore (1992) and present numerical results for both flow and deformation theories of plasticity

4. FEA results for Batterman's experiments

Figures 4.1 and 4.2 show that the buckling stresses calculated using the flow and deformation theories in the simulation of Batterman's tests display a low sensitivity to the imperfection amplitude for shells with $10 \leq R/t \leq 45$. However, both theories show an increase in the imperfection sensitivity for R/t ratios above 45. In particular, the flow and deformation theories of plasticity both overestimate the ultimate load for shells with $45 \leq R/t \leq 120$ if imperfections in the shells are not accounted for. On the other hand, both theories provide good agreement with experimental results if a 5% imperfection is included in the analysis.

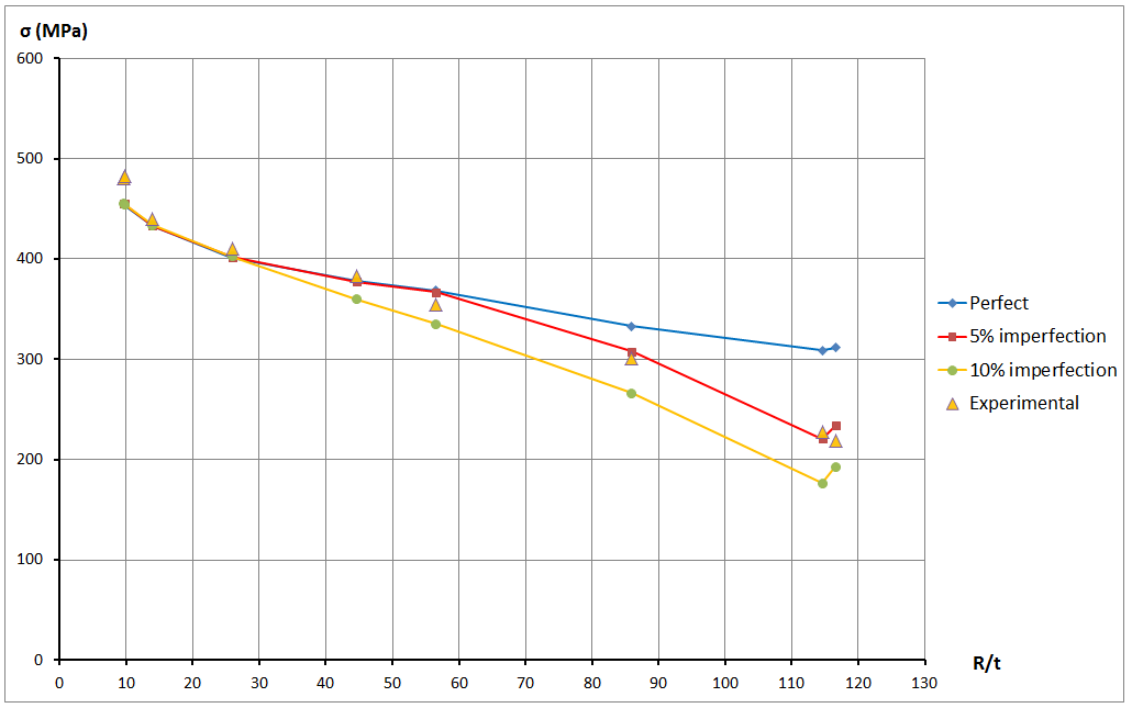

Figure 4.1: Imperfection sensitivity of buckling stress computed using the flow theory of plasticity.

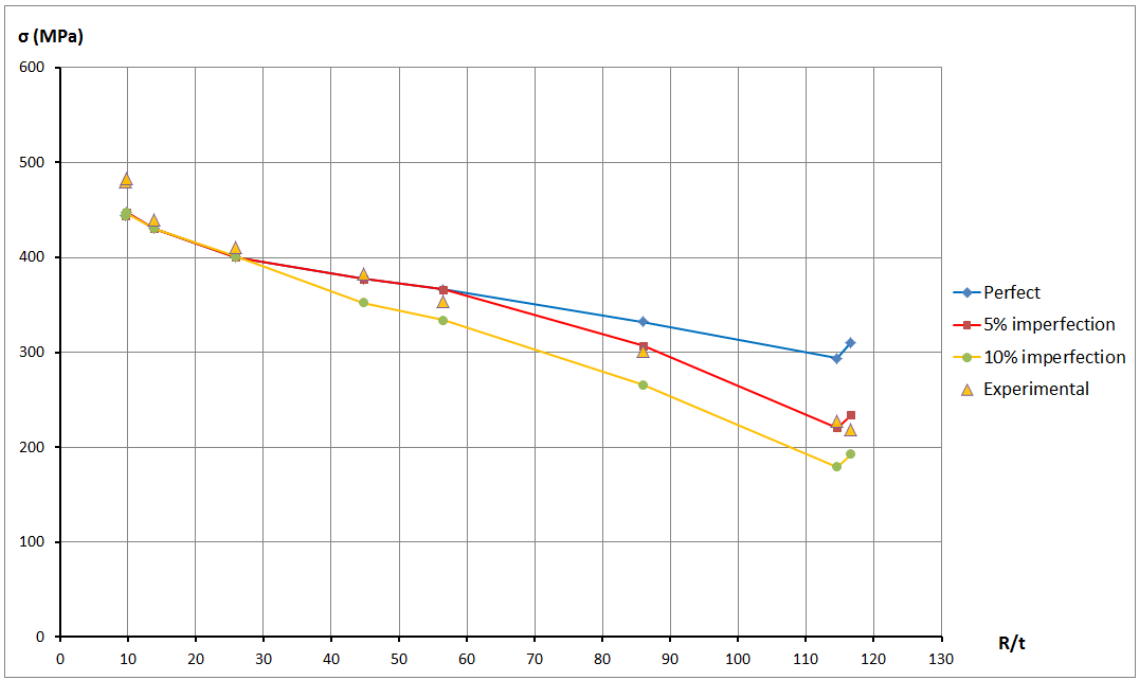

Figure 4.2: Imperfection sensitivity of buckling stresses computed using the deformation theory of plasticity.

It can be also noticed in Figures 4.1 and 4.2 that the differences between the calculations of buckling stresses using flow and deformation theories for perfect and imperfect cylinders are quite small both for thick and thin shells.

Spec.	Experimental Buckling Stress (Batterman, 1965)		Mode of failure predicted Numerically (Abaqus)					
	Buckling Stress (Mpa)	Mode of Failure	Flow Plasticity			Deformation Plasticity		
			perfect	5%	10%	perfect	5%	10%
12	480.08	AX Mode	AX, Ring-Shaped near the edges	AX, Ring-Shaped near the edges	AX, Ring-Shaped near the edges	AX, 3LW	AX, 3LW	AS, 3LW
18	482.63	AX Mode	AX, Ring-Shaped near the edges	AX, Ring-Shaped near the edges	AX, Ring-Shaped near the edges	AX, 3LW	AX, 3LW	AS, 3LW
22	439.8	AX Mode	AX, Ring-shaped at the central region	AX, Ring-shaped at the central region	AX, Ring-shaped at the central region	AX, Ring-shaped at the central region	AX, Ring-shaped at the central region	AX, Ring-shaped at the central region
5	410.72	AX Mode	AX, Ring-shaped at the central region	AX, Ring-shaped at the central region	AX, Ring-shaped at the central region	AX, Ring-shaped at the central region	AX, Ring-shaped at the central region	AX, Ring-shaped at the central region
15	382.6	AX Mode near ends, gentle DM pattern in central region	AX, 3LW	AX near the ends, gentle DM pattern in the central region	DM pattern in the central region	AX, 3LW	Ring-Shaped near the edges and DM pattern in the central region	DM pattern in the central region
16	354.25	DM pattern	AX, Ring-Shaped near the edges	DM pattern	DM pattern	AX, Ring-Shaped near the edges	DM pattern	DM pattern
26	301.23	DM pattern	AX, Ring-Shaped near the edges	DM pattern	DM pattern	AX, Ring-Shaped near the edges	DM pattern	DM pattern
8	227.73	DM pattern	AX, Ring-Shaped near the edges	DM pattern	DM pattern	AX, 5LW	DM pattern	DM pattern
9	219.05	DM pattern	AX, Ring-Shaped near the edges	DM pattern	DM pattern	AX, Ring-shaped at the central region	DM pattern	DM pattern

* AX-Axisymmetric buckling wave * AS- Almost axisymmetric buckling wave * DM-Diamond shaped buckling wave * LW- number of longitudinal waves

Table 4.1: Comparison between modes of failure numerically calculated and those experimentally observed by Batterman (1965).

Spec.	Experimental Buckling Stress (Batterman, 1965)	Numerical Analysis (ABAQUS)					
		Flow Plasticity			Deformation Plasticity		
		Buckling Stress (Mpa)	P_{expt}/P_{ABAQUS}	Mode of failure	Buckling Stress (Mpa)	P_{expt}/P_{ABAQUS}	Mode of failue
12	480.08	455.632	1.05	AX, Ring-Shaped near the edges	444.198	1.08	AX, 3LW
18	482.63	453.912	1.06	AX, Ring-Shaped near the edges	447.863	1.08	AX, 3LW
22	439.8	433.111	1.02	AX, Ring-shaped at the central region	430.336	1.02	AX, Ring-shaped at the central region
5	410.72	401.427	1.02	AX, Ring-shaped at the central region	400.203	1.03	AX, Ring-shaped at the central region
15	382.6	377.503	1.01	AX, 3LW	377.429	1.01	AX, 3LW
16	354.25	368.405	0.96	AX, Ring-Shaped near the edges	366.162	0.97	AX, Ring-Shaped near the edges
26	301.23	333.042	0.90	AX, Ring-Shaped near the edges	332.445	0.91	AX, Ring-Shaped near the edges
8	227.73	308.725	0.74	AX, Ring-Shaped near the edges	296.1	0.78	AX, 5LW
9	219.05	311.703	0.70	AX, Ring-Shaped near the edges	310.609	0.71	AX, Ring-shaped at the central region

Table 4.2: Compression between measured test results and corresponding numerical results for both flow and deformation theories of plasticity for perfect cylinders

Spec.	Experimental Buckling Stress (Batterman, 1965)	Numerical Analysis (ABAQUS)					
		Flow Plasticity			Deformation Plasticity		
		Buckling Stress (Mpa)	P_{expt}/P_{ABAQUS}	Mode of failure	Buckling Stress (Mpa)	P_{expt}/P_{ABAQUS}	Mode of failure
12	480.08	455.57	1.05	AX, Ring-Shaped near the edges	444.13	1.08	AX, 3LW
18	482.63	454.87	1.06	AX, Ring-Shaped near the edges	447.70	1.08	AX, 3LW
22	439.8	433.18	1.02	AX, Ring-shaped at the central region	430.38	1.02	AX, Ring-shaped at the central region
5	410.72	401.56	1.02	AX, Ring-shaped at the central region	400.36	1.03	AX, Ring-shaped at the central region
15	382.6	377.44	1.01	AX near the ends, gentle DM pattern in the central region	377.40	1.01	Ring-Shaped near the edges and DM pattern in the central region
16	354.25	366.92	0.97	DM pattern	366.25	0.97	DM pattern
26	301.23	307.92	0.98	DM pattern	306.92	0.98	DM pattern
8	227.73	220.93	1.03	DM pattern	220.84	1.03	DM pattern
9	219.05	234.04	0.94	DM pattern	234.03	0.94	DM pattern

Table 4.3: Compression between measured test results and numerical results for both flow and deformation theories of plasticity (5% imperfections)

Spec.	Experimental Buckling Stress (Batterman, 1965)	Numerical Analysis (ABAQUS)					
		Flow Plasticity			Deformation Plasticity		
		Buckling Stress (Mpa)	P_{expt}/P_{ABAQUS}	Mode of failure	Buckling Stress (Mpa)	P_{expt}/P_{ABAQUS}	Mode of failure
12	480.08	455.385	1.05	AX, Ring-Shaped near the edges	443.92	1.08	AS, 3LW
18	482.63	454.604	1.06	AX, Ring-Shaped near the edges	447.40	1.08	AS, 3LW
22	439.8	433.366	1.01	AX, Ring-shaped at the central region	430.51	1.02	AX, Ring-shaped at the central region
5	410.72	402.334	1.02	AX, Ring-shaped at the central region	400.83	1.02	AX, Ring-shaped at the central region
15	382.6	359.507	1.06	DM pattern in the central region	352.59	1.09	DM pattern in the central region
16	354.25	334.873	1.06	DM pattern	333.85	1.06	DM pattern
26	301.23	266.18	1.13	DM pattern	266.02	1.13	DM pattern
8	227.73	176.401	1.29	DM pattern	179.52	1.27	DM pattern
9	219.05	192.924	1.14	DM pattern	192.83	1.14	DM pattern

Table 4.4: Compression between measured test results and numerical results for both flow and deformation theories of plasticity (10% imperfections)

Table 4.1 shows that the presence of initial imperfections also affects the failure modes bringing them into closer agreement with the failure mode predicted experimentally.

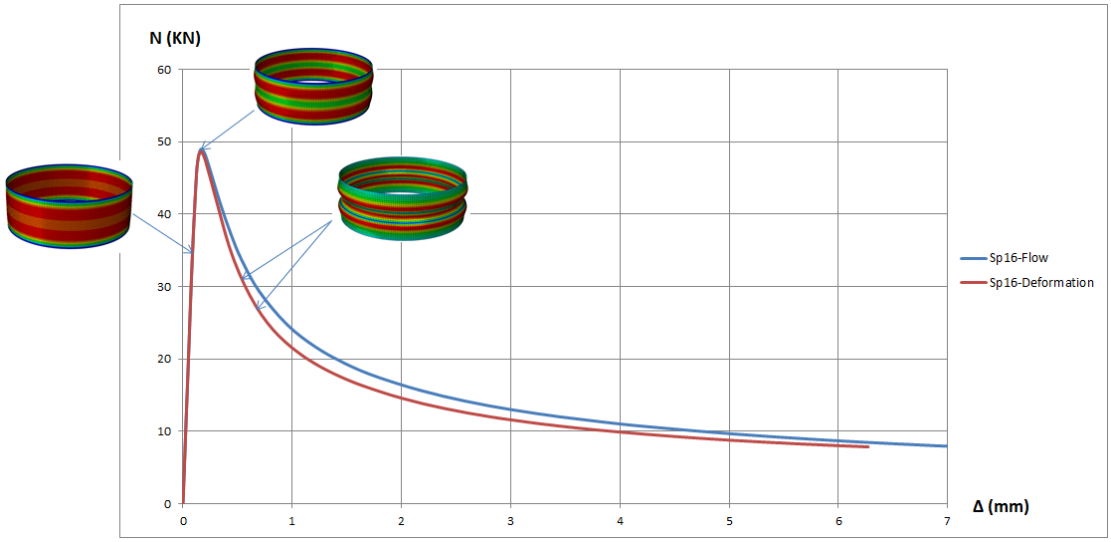

Figure 4.3: Axial load vs. prescribed displacement numerically predicted for specimen 16 for flow and deformation theory in the case of perfect geometry.

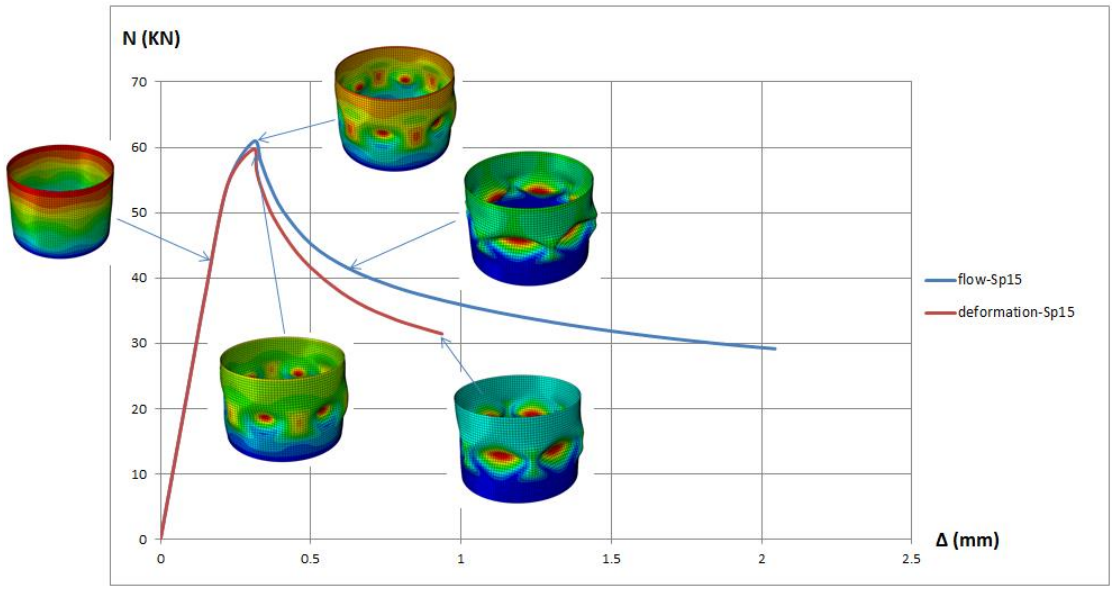

Figure 4.4: Axial load vs. prescribed displacement numerically predicted for specimen 15 for flow and deformation theory with an amplitude of initial imperfection equal to 10% of the thickness.

Figures 4.3-4.4 show the relation between axial loads and corresponding end shortening for specimens 15 and 16. The load-displacement curves obtained for all other specimens are very similar to those in Figures 4.3 and 4.4 and therefore have not

been reported. Again, it can be observed that for the various geometries and imperfections considered the curves predicted by the flow theory are always above those provided by the deformation theory.

5. Discussion and interpretation of FEA results in the context of the plastic buckling paradox

The main findings from the numerical results presented in Sections 3 and 4 are that:

(i) when correctly and accurately incorporated in accurate FE modelling, the deformation and flow theories of plasticity provide results which in general, and in particular in terms of buckling stresses, are similar and only occasionally differ more than 10%;

(ii) the flow theory of plasticity consistently provides results which are in closer agreement with the experimental data;

(iii) following the first part of the load-displacement curve in which the two theories essentially provide the same results, with increasing applied displacements the loads calculated using the flow theory becomes systematically larger than those obtained using by the deformation theory for all cases analysed.

The first two findings are in clear contrast with the conclusions of many authors, as discussed in Section 1. In particular, Tables 3.3 and 3.4 show very large discrepancies between the buckling stresses calculated using the present numerical simulations and those calculated analytically by Durban and Ore (1992) and Mao and Lu (1999)

The following sections present a comprehensive discussion on the possible causes for such discrepancy.

First a mesh-convergence analysis and the effects of the initial imperfections are examined and it is concluded that both have negligible effect on the findings. Second, it is shown that the analytical approaches provide, by their own nature, solutions that are kinematically over constrained and that, for this reason, lead to an over stiffened model both in the case of the flow and deformation theories of plasticity. Third, the influence of using the flow or the deformation theory of plasticity from the material standpoint is analysed with the help of a simplified model in the fashion of that proposed by Hutchinson (1972). This elementary model highlights in a very direct manner the influence of the different unloading paths on the results provided by the deformation

and the flow theories of plasticity and it clearly shows that the first underestimates buckling loads in comparison to the second.

It is thus concluded that using the deformation theory of plasticity in conjunction with a restrained kinematics, as it is the case of the analytical models, produces a compensation of two errors of different sign which, in the end, generally happens to yield results quite in line with the experimental findings.

5.1 Robustness of the FE model

A mesh-convergence analysis performed showed negligible changes in results by employing either coarser or and more refined meshes than those used to produce the presented results; additionally, a sensitivity analysis revealed that the results are not affected by the small numerical difference in the monotonic uniaxial stress-strain curve between the flow and the deformation theory of plasticity on account of setting $\bar{\sigma}(0) = 10^{-5}$ MPa instead of $\bar{\sigma}(0) = 0$ (see Section 2.1.2). Hence, it is concluded that there seems to be no particular issue with the accuracy of the FE modelling used here.

5.2 Influence of initial imperfections

With respect to the influence of initial imperfections, some authors recently suggested that, at least in the case of the analysis of lined pipes under compression, the overestimation of the buckling stress predicted by the flow theory can be reduced by giving the initial imperfections a certain amplitude (Hilberink et al., 2010). However, the results of the sensitivity analysis to imperfections reported in Sections 3 and 4 clearly show that not accounting for imperfections leads to an overestimation of the buckling stress which is very similar for both the flow and the deformation theory. In other words, for both sets of tests simulated in the present analyses erroneous consideration of imperfections would not lead to a larger overestimation of the buckling stress when using the flow theory than using the deformation theory of plasticity.

5.3 Buckling shapes and over-constraint of analytical models

The implicit kinematic constraint in assuming a certain buckling shape as the basis of analytical models seems to be the main reason for the discrepancy between the presented numerical results and the analytical findings which have suggested the existence of a plastic buckling paradox. Actually, it is on the basis of the results from

several analytical calculations that it is widely accepted that the flow theory leads to a significant overestimation of the buckling stress while the deformation theory provides much more accurate prediction and is therefore recommended for use in practical applications (see, for example, Mao and Lu (2001, 2002)).

Actually, the buckling shapes determined by the inherent simplifications of the analytical treatments result in kinematic constraints which yield a stiffer structural response and, as a consequence, an overestimation of the buckling stress.

Batterman (1965) derived analytical equations to define the buckling stress and corresponding number of half wave (m) for flow and deformation theories of plasticity. He assumed simply supported boundary conditions and the stress-strain relationship of the material was represented by the Ramberg-Osgood expression. The expressions of the buckling stresses obtained in the case of the flow and deformation theories are reported in Appendix A. They were derived from an axisymmetric buckling shape in the form

$$v_n = A\sin\left(m\pi x / L\right) \tag{5-1}$$

Table 5.1 shows the maximum buckling stress for each specimen of Lee's cylindrical shells and its corresponding number of half waves m. It can be seen that the corresponding number of half waves predicted by flow theory of plasticity is very different from that predicted by the deformation theory of plasticity and therefore the maximum buckling stress predicted also differs sensibly. Further validation of these results is given by the fact that the maximum buckling stresses are almost equal to buckling stresses calculated by Durban and Ore (1992) (Table 3.4).

Spec.	Experimental buckling stress (MPa)	Analytical predictions			
		m (Flow)	σ (Flow)	m (Def.)	σ (Def.)
A330	96.87	3	165.6	7	89.85
A320	78.6	5	124.2	11	74.63
A220	81.15	7	125.05	17	74.63
A310	64.74	7	105.74	13	67.23
A110	74.12	17	105.75	33	67.23
A300	69.71	9	88.75	17	59.78

Table 5.1: The maximum buckling stress and corresponding number of half-waves obtained analytically

Cylindrical test specimens have been modelled here using finite-element modelling based on a 2-node linear axisymmetric shell element (named SAX1 in ABAQUS), with a uniform mesh.

In order to reproduce the shape from the analytical solution presented in Table 5.1, the cylinders were partitioned into an appropriate number of parts, corresponding to the number of half waves yielded by the analytical solution, by using the edge partition tool in ABAQUS. Each part was meshed into ten elements. Linear constraint equations were used to ensure that radial displacement of the nodes replicated the desired number of half-waves.

This is shown, for example, in Figure 5.1.

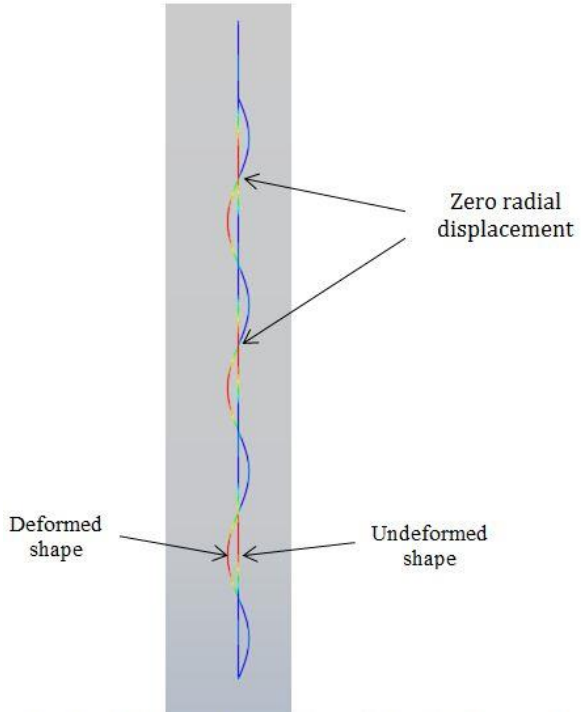

Figure 5.1: Deformed and undeformed shape of the cylinder for the case of m=7

Table 5.2 shows the comparison between the maximum buckling stresses obtained analytically and numerically with and without the use of equation constraints for a number of specimens.

It is evident that imposing constraint equations on the FE model in order to reproduce the shape of the analytical solution makes the buckling stresses predicted by the flow theory of plasticity well in excess of those predicted by the deformation theory of plasticity. The latter coincidentally seem therefore to be in better agreement with the experimental results.

Spec.	Experimental buckling stress (MPa)	Analytical predictions				Numerical (FE+ kinematical constraints)		Numerical using S4 element (Without kinematical constraints)		Numerical using SAX1 element (Without kinematical constraints)	
		m (Flow)	σ (Flow)	m (Def.)	σ (Def.)	σ (Flow)	σ (Def.)	σ (Flow)	σ (Def.)	σ (Flow)	σ (Def.)
A330	96.87	3	165.6	7	89.85	151.77	101.3	98.58	88.82	92.64	85.20
A320	78.6	5	124.2	11	74.63	121.9	83.4	80.48	74.10	74.72	69.58
A220	81.15	7	125.05	17	74.63	136.67	84.42	80.85	73.90	74.74	69.57
A310	64.74	7	105.74	13	67.23	106.13	75.28	72.47	66.84	66.59	62.29
A110	74.12	17	105.75	33	67.23	121.23	76.78	72.94	66.84	66.63	62.29
A300	69.71	9	88.75	17	59.78	94.95	66.66	64.25	59.16	58.55	55.03

Table 5.2: Comparison between the buckling stress obtained analytically and numerically with and without the use of equation constraints

On the other hand, without any constraints on the displacements the results from using the flow theory of plasticity in the S4 elements are, as pointed out in the previous sections, in much better agreement with the experimental results than those by use of the deformation theory. Using SAX1 axisymmetric elements without kinematic constraints confirms this fact, but in such a case the results from deformation theory tend to underestimate the buckling stresses even more than in the case of the S4 elements.

Overall, it can be concluded that the use of the deformation theory tends to underestimate the buckling load and this fact, in the case of the analytical solution proposed by Batterman, compensates the over stiffened kinematics from the simplified analytical equations.

In the next section it is shown that the underestimation of the buckling stress produced by the deformation theory of plasticity may be essentially attributed to the incorrect modelling of the actual unloading path.

5.4 Effects of unloading: analysis through a semi-analytical model

It is worth recalling that the fundamental differences between flow and deformation theories lie in the stress-strain responses (i) during non-proportional loading and (ii) during unloading.

Plastic buckling does indeed lead to non-proportional loading because before the onset of plasticity strains are elastic whereas, once the stress reaches and exceeds the yield strength, plastic strains gradually become predominant. Since the rate of plastic strain is normal to the yield domain, typically the strain path deviates significantly from the initial straight line followed during elastic loading. This aspect is captured in the same manner by the constitutive relationships used in the performed numerical FE analyses and in the analytical formulations.

On the other hand, unloading is correctly represented by the use of the flow theory in the present numerical calculations, but it is physically misrepresented in the analytical investigations. In the following, by means of a simplified model and semi-analytical calculations it is shown that, because of this, the deformation theory intrinsically tends to under predict the buckling load.

In order to isolate the role played by the different stress responses resulting from the use of the flow or the deformation theory after strain reversal, i.e. material unloading, a simplified model conceptually similar to the one proposed by Hutchinson (1972) is considered. The model qualitatively reproduces the geometrically nonlinear response of a cylinder in compression and is modelled by uniaxial stress-strain relationships, leading by definition to proportional (material) loading.

The model is described in in Figure 5.2: it consists of two rigid bars connected by two pin-ended short struts. Suffixes 1 and 2 are used to denote the lower and upper central struts. Each rigid bar has length equal to $a - h$ and a rectangular cross section of depth d and width c, whereby the cross section area is $A = c\ d$. The short struts have length $2h$ and cross sectional areas equal to $A_1 = A_2 = A/2$.

The structure is axisymmetrically supported and subjected to an end-load P with an eccentricity e. Moreover, nonlinear elastic 'unstable' springs are assumed to act orthogonally to the rigid bars. They are introduced to account for geometric nonlinearity effects and are characterized by a nonlinear and de-stabilizing response. The responses of the springs are unstable in the sense that the force transmitted is in the same direction as the spring deformation rather than opposite to it, i.e. tensile for spring elongation and compressive for spring shortening, in accordance with the following formula

$$Q = c\ \beta\ \Delta^2\ \mathrm{sign}(\Delta) \tag{5.2}$$

where Q is the force, Δ is the lateral displacement (spring elongation) and β is the material constant of the spring.

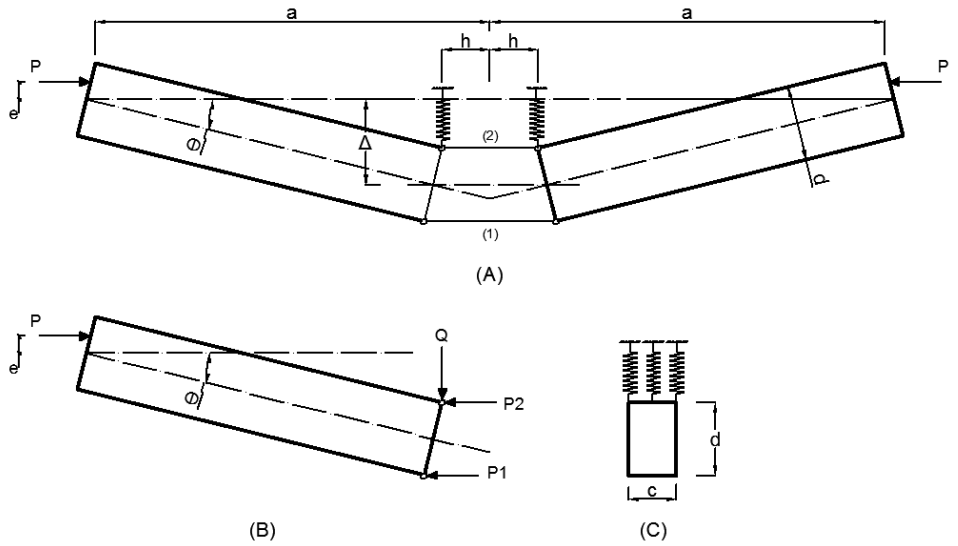

Figure 5.2: A simplified model after Hutchinson (1972)

Essentially, the presence of these nonlinear and unstable springs qualitatively reproduces the unstable post-buckling responses due to the peculiar geometrically nonlinear nature of structures, such cylinders in compression, via the introduction of material nonlinearity and unstable structural components. Geometrical nonlinearity is translated into material nonlinearity, which enables a study of the pre- and post-buckling response of the structure with a simple second-order approach, resulting in relatively easy analytical computations.

The stresses and strains in the struts are taken as positive when compressive. Denoting the strain in the struts by ε_1 and ε_2, the rotation of the left hand bar is given by

$$\theta = \frac{h(\varepsilon_2 - \varepsilon_1)}{d} \tag{5.3}$$

From Figure 5.2, the lateral displacement Δ is:

$$\Delta = (a - h)\,\theta = (a - h)\frac{h(\varepsilon_2 - \varepsilon_1)}{d} \tag{5.4}$$

The stress-strain relation is in the form of a bilinear elastic-plastic behavior with isotropic hardening which can be expressed as

$$\begin{cases} \sigma_1 = a_1 + b_1\,\varepsilon_1 \\ \sigma_2 = a_2 + b_2\,\varepsilon_2 \end{cases} \tag{5.5}$$

where a_i and b_i, i = 1,2, are material constants that depend on the (linear) branch of the stress-strain curve and on whether the deformation or the flow theory of plasticity is used, as shown in Figure 5.3.

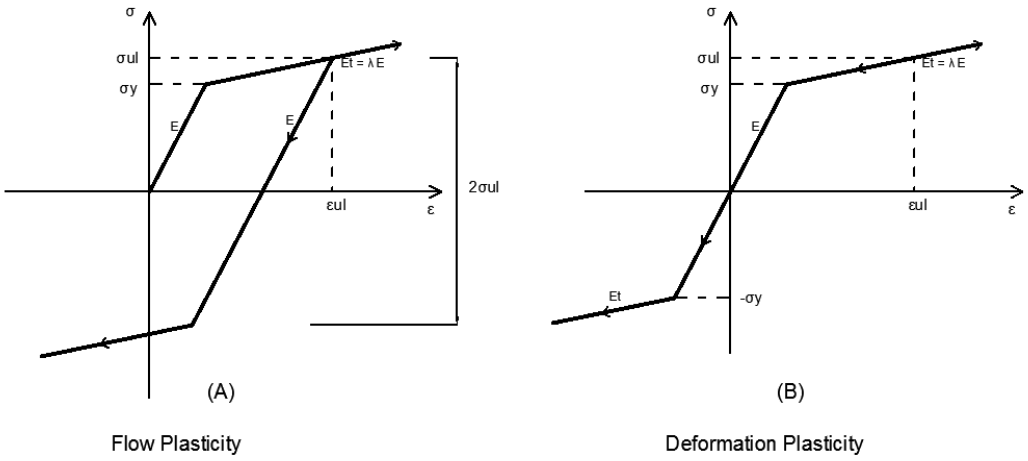

Figure 5.3: Bilinear stress-strain curves used for the flow and deformation theory.

Equilibrium requires that

$$P_1 + P_2 = P \tag{5.6}$$

where

$$\begin{cases} P_1 = A_1\,\sigma_1 = \frac{1}{2}A\,\sigma_1 = \frac{1}{2}d\,c\,\sigma_1 \\ P_2 = A_2\,\sigma_2 = \frac{1}{2}A\,\sigma_2 = \frac{1}{2}d\,c\,\sigma_2 \end{cases} \tag{5.7}$$

Equilibrium about any point along the line of action of P yields

$$\mathrm{P}_1(\Delta + e + d/2) + \mathrm{P}_2(\Delta + e - d/2) + (a - h)\,c\,\beta\Delta^2 = 0 \tag{5.8}$$

And from Equation (5.4), one has

$$\varepsilon_2 - \varepsilon_1 = \frac{\Delta}{a-h}\frac{d}{h} \tag{5.9}$$

By defining

$$x = \varepsilon_2 - \varepsilon_1 \quad \text{and} \quad \sigma = (\sigma_1 + \sigma_2)/2 \tag{5.10}$$

and solving for σ leads to:

$$\sigma = \frac{\mathrm{a_2 b_1} d^2 - a_1 b_2 d^2 + b_1 b_2 d^2 x + 2a b_1 \beta\Delta^2 + 2a b_2 \beta\Delta^2 - 2 b_1 h \beta\Delta^2 - 2 b_2 h \beta\Delta^2}{d(b_2(-d+2(e+\Delta)) + b_1(d+2(e+\Delta)))} \tag{5.11}$$

The horizontal deflection of the point where the load P is applied can be calculated:

$$u = \frac{(\varepsilon_1+\varepsilon_2)h}{2} + a\,e\,\theta + a(1-cos\theta) \tag{5.12}$$

In order to determine the relation between stress σ and the deflection Δ or the longitudinal displacement u the following procedure is used.

The value of deflection Δ is incrementally increased and σ and x and are calculated from Equations (5.9)-(5.11). The strains $\varepsilon_1, \varepsilon_2$, stresses σ_1, σ_2 and the horizontal deflection u are then evaluated. At each increment, the loading stage of each strut on the stresses-strain curve (Figure 5.3) is determined based on its stresses σ_1, σ_2. The coefficients a_1, a_2, b_1, b_2 are then calculated according to the current loading stage and to the plasticity theory adopted in accordance with Tables 5.3 and 5.4.

Loading stage		**Strut 1**	**Strut 2**
1	Both struts are elastic	$a_1 = 0$ $b_1 = E$	$a_2 = 0$ $b_2 = E$
2	Strut 2 plastic, strut1 elastic	$a_1 = 0$ $b_1 = E$	$a_2 = \sigma_y(1-\lambda)$ $b_2 = \lambda E$
3	Both struts plastic	$a_1 = \sigma_y(1-\lambda)$ $b_1 = \lambda E$	$a_2 = \sigma_y(1-\lambda)$ $b_2 = \lambda E$
4	Strut 1 elastic unloading, Strut 2 plastic loading	$a_1 = \sigma_{ul} - E\varepsilon_{ul}$ $b_1 = E$	$a_2 = \sigma_y(1-\lambda)$ $b_2 = \lambda E$
5	Strut 1 plastic reloading, Strut 2 plastic loading	$a_1 = \sigma_{ul}(2\lambda-1) - \lambda E\varepsilon_{ul}$ $b_1 = \lambda E$	$a_2 = \sigma_y(1-\lambda)$ $b_2 = \lambda E$

Table 5.3: loading stages in the case of flow plasticity.

The procedure was implemented in a FORTRAN code and analyses were conducted assuming $a = 250$ mm , $d = 15$ mm, $h = 5$ mm. The cross section of the rigid bar was assumed to be square. The material properties for the struts were assumed to be $\sigma_y = 100$ MPa, $E = 70000$ MPa and $\lambda = 0.5$. The nonlinear spring constant was assumed equal to $\beta = 10$ Nmm^{-3} and two values of load eccentricity considered in the calculations were, $e = 0.5$ mm , $e = 2$ mm. The results are reported in Figures 5.4-5.7.

It is evident from the $P-u$ and $P-\Delta$ plots that both theories of plasticity provide the same results up to the onset of stage 3 (i.e. start of unloading in one strut). From

that point on the deformation theory of plasticity underestimates the carried load by up to 20% with respect to the corresponding load calculated using the flow theory, depending on the value of the assumed imperfection.

This fact provides a direct and physical explanation to the findings from analytical and FE analyses and supports the hypothesis that adopting the deformation theory of plasticity is likely to counterbalance the excessive structural stiffness resulting from assumed buckling modes, thus providing results that are seem only coincidentally to be more in line with the experimental findings.

Loading stage		**Strut 1**	**Strut 2**
1	Both struts are elastic	$a_1 = 0$ $b_1 = E$	$a_2 = 0$ $b_2 = E$
2	Strut 2 plastic, strut1 elastic	$a_1 = 0$ $b_1 = E$	$a_2 = \sigma_y(1-\lambda)$ $b_2 = \lambda E$
3	Both struts plastic	$a_1 = \sigma_y(1-\lambda)$ $b_1 = \lambda E$	$a_2 = \sigma_y(1-\lambda)$ $b_2 = \lambda E$
4	Strut 1 plastic unloading, strut 2 plastic loading	$a_1 = \sigma_{ul} - \lambda E \varepsilon_{ul}$ $b_1 = \lambda E$	$a_2 = \sigma_y(1-\lambda)$ $b_2 = \lambda E$
5	Strut 1 elastic unloading, strut 2 plastic loading	$a_1 = 0$ $b_1 = E$	$a_2 = \sigma_y(1-\lambda)$ $b_2 = \lambda E$
6	Strut 1 plastic reloading, strut 2 plastic loading	$a_1 = \sigma_y(\lambda-1)$ $b_1 = \lambda E$	$a_2 = \sigma_y(1-\lambda)$ $b_2 = \lambda E$

Table 5.4: loading stages in the case of deformation plasticity.

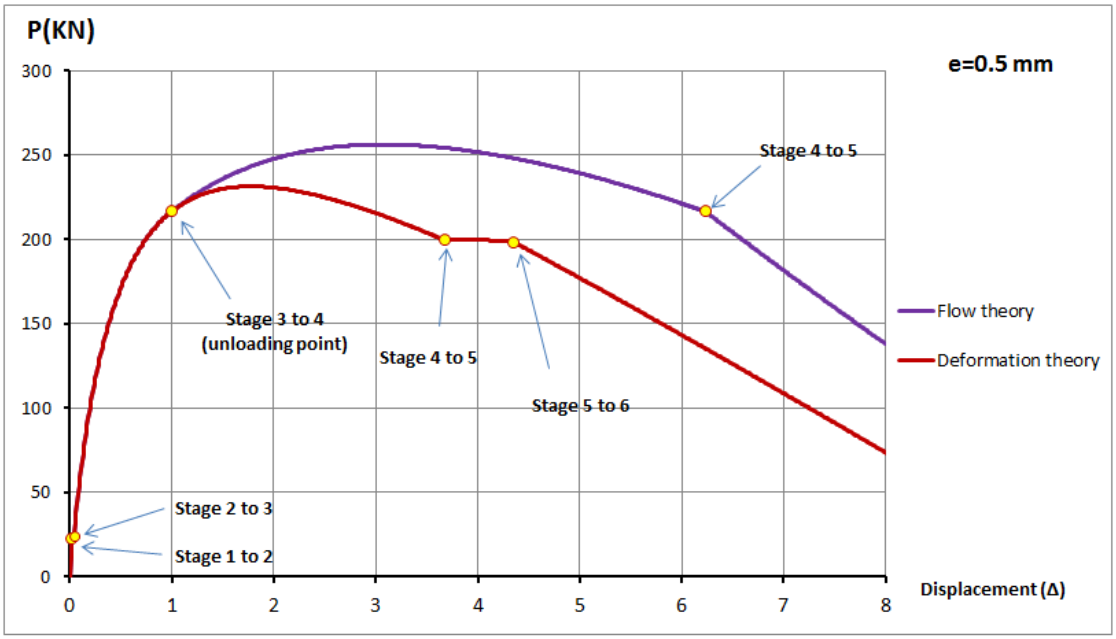

Figure 5.4: $P-\Delta$ plot from the simplified model: comparison between flow and deformation theory, $e = 0.5$ mm.

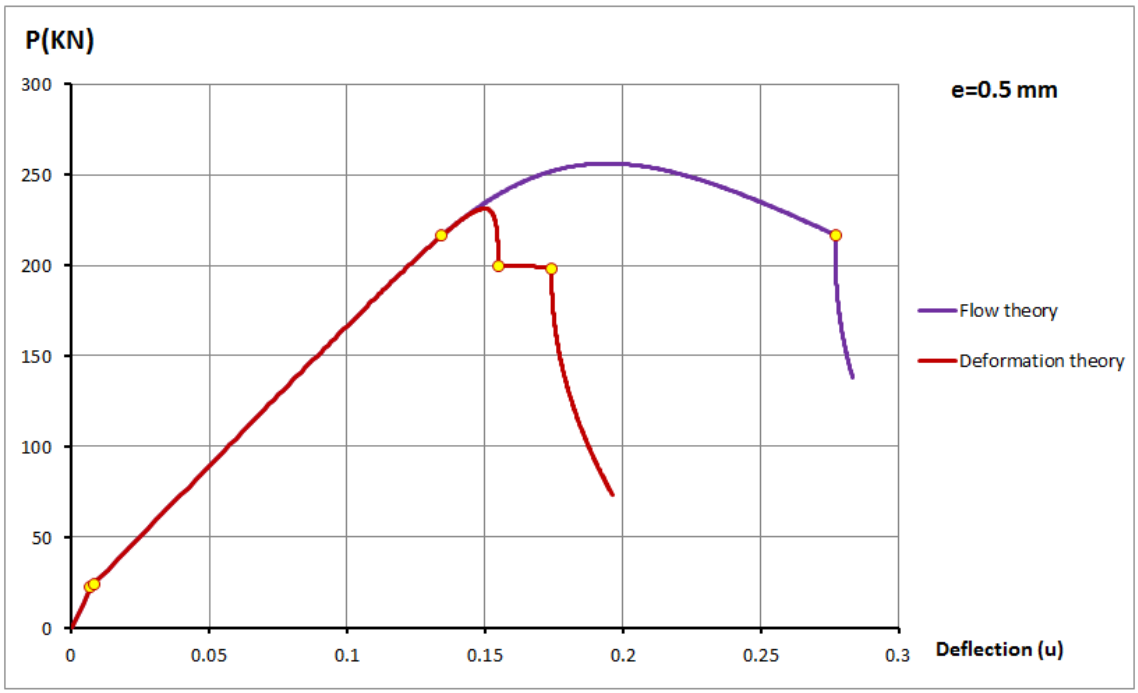

Figure 5.5: $P-u$ plot from the simplified model: comparison between flow and deformation theory, $e = 0.5$ mm.

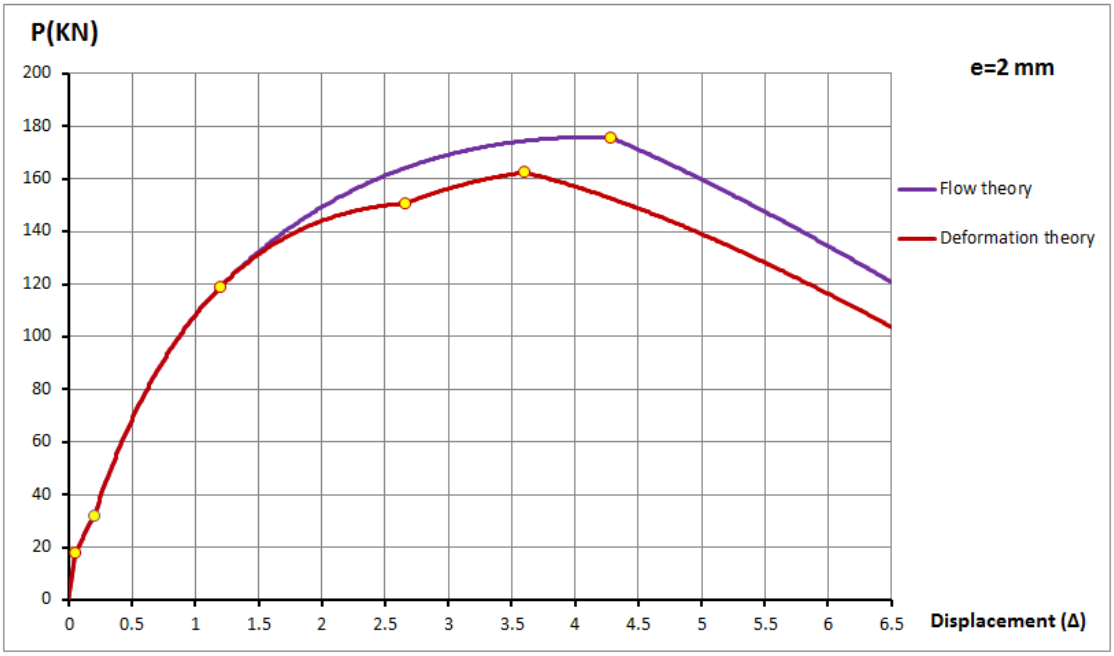

Figure 5.6: $P - \Delta$ plot from the simplified model: comparison between flow and deformation theory, $e = 2$ mm.

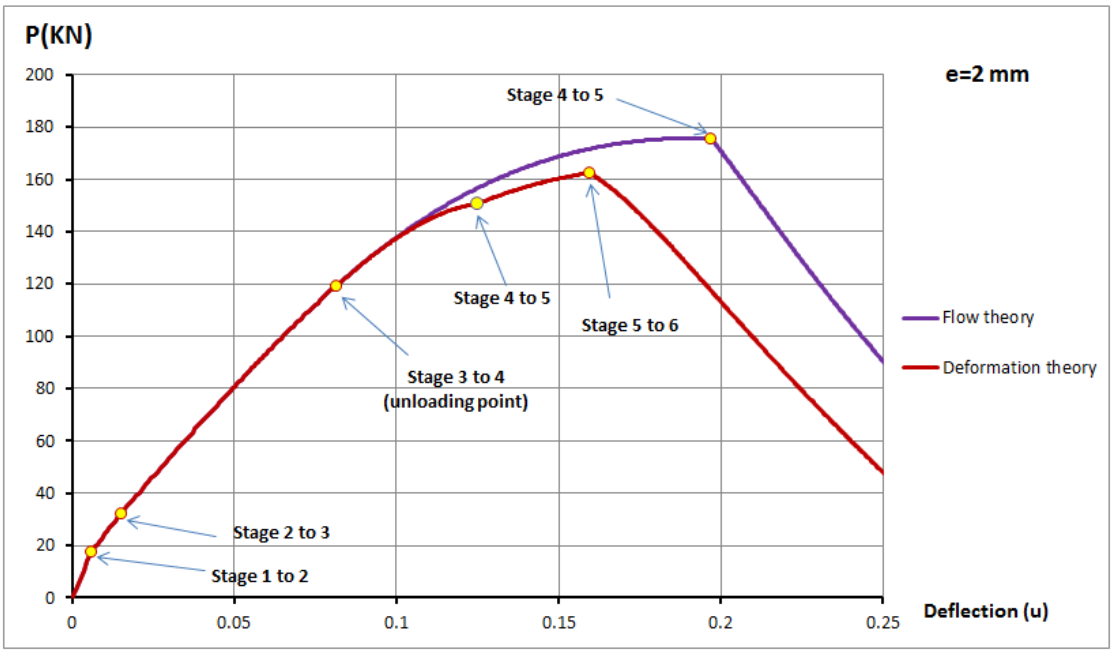

Figure 5.7: $P - u$ plot from the simplified model: comparison between flow and deformation theory, $e = 2$ mm.

6. Conclusions

The discrepancy between the presented results and those in the literature by many other authors can be summarised by stating that, according to the performed numerical investigations in the cases under consideration here there is actually no plastic buckling paradox. In fact, the flow theory of plasticity, which provides a physically sound

description of the behaviour of metals, leads to predictions of the buckling stress which are in better agreement with the corresponding test results than those provided by use of the deformation theory.

This is in contrast to the conclusions by other authors and with the widely accepted belief that the flow theory leads to a significant overestimation of the buckling stress while the deformation theory leads to much more accurate predictions and, therefore, is the recommended choice for use in practical applications. The reason for these different conclusions has been carefully investigated from different standpoints and with the help of simplified models.

The roots of the discrepancy are found in the simplifying assumptions with regards to assumed buckling modes used as the basis of many analytical investigations and essentially in the fact that adopting the deformation theory of plasticity contributes to counterbalance the excessive stiffness induced by kinematically constraining the cylinders to follow predefined buckling modes, thus providing results that are only apparently more in line with the experimental findings.

Additional numerical and experimental work would be expedient in order to extend the analysis to cylinders subjected to axial compression but made of materials different from aluminium, as well as to other structures or loading conditions. This course of action would be also beneficial in order to inform changes in the current design standards regarding buckling calculations based on analytical or FEA.

References

The first author would like to gratefully acknowledge the financial support from the Damascus University.

References

Batterman, S.C. (1965). Plastic buckling of axially compressed cylindrical shells. *AIAA Journal*, 3(2):316-325.

Bardi, F.C. and Kyriakides, S. (2006). Plastic buckling of circular tubes under axial compression - Part I: Experiments. *International Journal of Mechanical Sciences*, 48(8):830-841.

Blachut, J., Galletly, G.D and James, S. (1996). On the plastic buckling paradox for cylindrical shells. *Proceedings of the Institution of Mechanical Engineers, Part C*, 210(5):477-488.

Galletly G.D., Blachut, J., and Moreton, D.N. (1990). Internally pressurized machined domed ends - a comparison of the plastic buckling predictions of the deformation and

flow theories. *Proceedings of the Institution of Mechanical Engineers, Part C*, 204(2):169-186.

Bushnell, D. (1982). Plastic Buckling, in *Pressure Vessels and Piping: Design Technology – 1982, A Decade of Progress*, edited by Zamrik, S. Y. and Dietrich, D. American Society of Mechanical Engineers, New York, 47-117.

Bushnell, D. (1986). BOSOR5 – Program for Buckling of Complex, Branched Shells of Revolution Including Large Deflections, Plasticity and Creep. In *Structural Analysis Systems – Vol. 2*, edited by Niku-Lari, A. Pergamon, 25-54.

Falzon, B.G. (2006). An Introduction to Modelling Buckling and Collapse. Glasgow, UK, NAFEMS Ltd

Hilberink, A., Gresnigt, A.M. and Sluys, L.J. Liner wrinkling of lined pipe under compression. A numerical and experimental investigation. *Proceedings of the ASME 29th International Conference on Ocean, Offshore and Arctic Engineering OMAE 2012* Shanghai, China, June 6-11,2010.

Hutchinson, J.W. (1972) On the postbuckling behavior of imperfection-sensitive structures in the plastic range. *Journal of Applied Mechanics – Transactions of ASME*, 39:155–162.

Hutchinson, J. W. (1974). Plastic Buckling. *Advances in Applied Mechanics*, 14(67).

Lee, L. (1962). Inelastic buckling of initially imperfect cylindrical shells subjected to axial compression. *Journal of Aerospace Science*, 29:87-95.

Mao, R. and Lu, G. (1999). Plastic buckling of circular cylindrical shells under combined in-plane loads, *International Journal of Solids and Structures*, 38(5):741-757.

Mao, R. and Lu, G. (2001). A study of the plastic buckling of axially compressed cylindrical shells with a thick-shell theory, *International Journal of Mechanical Sciences*, 43(10):2319-2330.

Mao, R. and Lu, G. (2002). A study of elastic-plastic buckling of cylindrical shells under torsion, *Thin-Walled Structures*, 40(12):1051-1071.

Onat, E. T. and Drucker, D. C. (1953). Inelastic instability and incremental theories of

plasticity. *Journal of the Aeronautical Sciences*, 20: 181-186.

Ore, E. and Durban, D. (1992). Elastoplastic buckling of axially compressed circular cylindrical shells. *International Journal of Mechanical Sciences*, 34(9):727-742.

Riks, E. (1979). An incremental approach to the solution of snapping and buckling proplems. *International Journal of Solids and Structures*. 15(7): 529-551.

Sewell, M. J. (1963). A gerneral theory of elastic and inelastic plate failure-I. *Journalof the Mechanics and Physics of Solids*, 11 377-393.

Sewell, M. J. (1973). A yield-surface corner lowers the buckling stress of an elasticplasticplate under compression. *Journal of the Mechanics and Physics of Solids*, 21: 19-45.

Simo J.C. and Hughes T.J.R. (1998). *Computational Inelasticity*. Springer.

Simulia (2011). *ABAQUS Theory Manual*. Version 6.11-1. Dassault Systems.

Wang, X. and Huang, J. (2009). Elastoplastic buckling analyses of rectangular plates under biaxial loadings by the differential quadrature method. *Thin-Walled Structures*, 47(1):14-20.

Wang, X. and Zhang, W. (2011). Elastoplastic buckling analyses of thick rectangular using the differential quadrature method. *Computers and Mathematics with Applications*, 61(1):44-61.

Appendix

A1. Equations used for the deformation theory of plasticity

The extension of the Ramberg-Osgood law (2.1) to the case of a multi-axial stress state using the von Mises formulation (J_2 theory) results in the following path-independent relationship (Simulia, 2011) governing the deformation theory of plasticity:

$$E\boldsymbol{\varepsilon} = (1+\nu)\ \mathrm{dev}\,\boldsymbol{\sigma} - (1+2\nu)\ \mathrm{sph}\,\boldsymbol{\sigma} + \frac{3}{2}\alpha\left(\frac{\sqrt{\frac{3}{2}}\,\|\mathrm{dev}\,\boldsymbol{\sigma}\|}{\sigma_y}\right)^{n-1}\ \mathrm{dev}\,\boldsymbol{\sigma} \tag{A.1}$$

where $\boldsymbol{\varepsilon}$ and $\boldsymbol{\sigma}$ denote the strain and stress tensors, and dev $\boldsymbol{\sigma}$ and sph $\boldsymbol{\sigma}$ denote the deviatoric and spherical parts of the stress tensor, respectively.

Since the deformation theory of plasticity requires the same input values as the Ramberg-Osgood formula with the sole addition of the Poisson's ratio, the material constants of Table 2.5 have been used.

A2. Equations used for the flow theory of plasticity

The J_2 flow theory of plasticity theory (Simo and Hughes, 1998; Simulia, 2011), available in ABAQUS and used in the numerical simulations, is based on the additive decomposition of the spatial rate of the deformation tensor $\dot{\boldsymbol{\varepsilon}}$ into its elastic and plastic parts $\dot{\boldsymbol{\varepsilon}}_{\boldsymbol{e}}$ and $\dot{\boldsymbol{\varepsilon}}_{\boldsymbol{p}}$, respectively,

$$\dot{\boldsymbol{\varepsilon}} = \dot{\boldsymbol{\varepsilon}}_{\boldsymbol{e}} + \dot{\boldsymbol{\varepsilon}}_{\boldsymbol{p}} \tag{A.2}$$

The rate of the Cauchy stress tensor $\dot{\boldsymbol{\sigma}}$ is obtained from the elastic part of the strain tensor through the isotropic linear elastic relation

$$\dot{\boldsymbol{\sigma}} = 2G\dot{\boldsymbol{\varepsilon}}_{\boldsymbol{e}} + \mu\ \mathrm{tr}\,\dot{\boldsymbol{\varepsilon}}_{\boldsymbol{e}}\,\mathbf{I} \tag{A.3}$$

where G and μ are Lamé's elastic constants and $\mathbf{I}$ is the rank-2 identity tensor.

The von Mises yield function f is

$$f\left(\boldsymbol{\sigma}, \varepsilon_p^{eq}\right) = \|\mathrm{dev}\,\boldsymbol{\sigma}\| - \sqrt{\frac{2}{3}}\,\bar{\sigma}\left(\varepsilon_p^{eq}\right) \tag{A.4}$$

where $\bar{\sigma}$ represents the uniaxial yield strength which, in order to model nonlinear isotropic hardening, is assumed to be an increasing function of the equivalent plastic strain ε_p^{eq}, defined at time t as follows

$$\varepsilon_p^{eq}(t) = \int_{-\infty}^{t} \left\| \dot{\boldsymbol{\varepsilon}}_p(\tau) \right\| d\tau \tag{A.5}$$

The evolution of the plastic strain is given by the associated flow rule:

$$\dot{\boldsymbol{\varepsilon}}_p = \dot{\lambda} \left(\frac{\partial f}{\partial \boldsymbol{s}} \right)_{\boldsymbol{s}=\mathrm{dev}\,\boldsymbol{\sigma}} \tag{A.6}$$

where $\dot{\lambda}$ is a plastic multiplier which must satisfy the complementarity conditions:

$$\dot{\lambda} \geq 0 \qquad f\left(\boldsymbol{\sigma}, \varepsilon_p^{eq}\right) \leq 0 \qquad \dot{\lambda}\, f\left(\boldsymbol{\sigma}, \varepsilon_p^{eq}\right) = 0 \tag{A.7}$$

A3. Analytically derived buckling formulas derived by Batterman

The buckling stresses were analytically derived by Batterman (1965) in the following manner. In the case of the flow theory of plasticity the buckling stress is denoted by σ_f and the following expression was obtained:

$$\sigma_f = \frac{k\,(A + B - C)}{D} \tag{A.8}$$

with

$$\begin{aligned} k &= L^4(\lambda(5-4\upsilon) - (1-2\upsilon)^2) \qquad A = \frac{4E^2h^2m^2\pi^2\lambda(3+\lambda)}{L^2R^2(\lambda(5-4\upsilon)-(1-2\upsilon)^2)^2} \\ B &= \frac{E^2h^4m^6\pi^6(3+\lambda)^2}{12L^6(\lambda(5-4\upsilon)-(1-2\upsilon)^2)^2} \qquad C = \frac{4E^2h^2m^2\pi^2(-1+\lambda+2\upsilon)^2}{L^2R^2(\lambda(5-4\upsilon)-(1-2\upsilon)^2)^2} \\ D &= Eh^2m^4\pi^4(3+\lambda) \end{aligned} \tag{A.9}$$

where h, R, L, m are the thickness, radius, length of the cylinder and number of half waves, respectively, $\lambda = E/E_t$, E_t being tangent modulus of the material evaluated at stress level σ on a uniaxial stress-strain test curve and E being the elastic Young's modulus.

In the case of the deformation theory of plasticity the buckling stress is denoted by σ_d and the following expression was obtained:

$$\sigma_d = \frac{\bar{k}\,(\bar{A} + \bar{B} - \bar{C})}{\bar{D}} \tag{A.10}$$

with

$$\bar{k} = L^4(-(1-2\upsilon)^2 + \lambda(2-4\upsilon+3\psi)) \qquad \bar{A} = \frac{E^2h^4m^6\pi^6(\lambda+3\psi)^2}{12L^6(-(1-2\upsilon)^2+\lambda(2-4\upsilon+3\psi))^2}$$

$$\bar{B} = \frac{4E^2h^2m^2\pi^2\lambda(\lambda+3\psi)}{L^2R^2(-(1-2\upsilon)^2+\lambda(2-4\upsilon+3\psi))^2} \qquad \bar{C} = \frac{4E^2h^2m^2\pi^2(-1+\lambda+2\upsilon)^2}{L^2R^2(-(1-2\upsilon)^2+\lambda(2-4\upsilon+3\psi))^2} \tag{A.11}$$

$$\bar{D} = Eh^2m^4\pi^4(\lambda+3\psi)$$

where $\Psi = E/E_s$, E_s being the secant modulus of the material evaluated at stress level σ on a uniaxial stress-strain test curve.